PERGAMON

Computers & Fluids 31 (2002) 269–308

computers & fluids

www.elsevier.com/locate/compfluid

On the combined performance of nonlocal artificial boundary conditions with the new generation of advanced multigrid flow solvers ☆

T.W. Roberts [a], D. Sidilkover [b], S.V. Tsynkov [c,*]

[a] *Computational Modeling and Simulation Branch, MS 128, NASA Langley Research Center, Hampton, VA 23681-2199, USA*

[b] *ICASE, MS 132C, NASA Langley Research Center, Hampton, VA 23681-2199, USA*

[c] *School of Mathematical Sciences, Tel Aviv University, Ramat Aviv, Tel Aviv 69978, Israel*

Received 25 April 2000; accepted 23 April 2001

Abstract

We develop theoretically and implement numerically a unified flow solution methodology that combines the advantages relevant to two independent groups of methods in computational fluid dynamics that have recently proven successful: The new factorizable schemes for the equations of hydrodynamics that facilitate the construction of optimally convergent multigrid algorithms, and highly accurate global far-field artificial boundary conditions (ABCs). The primary result that we have obtained is the following. Global ABCs do not hamper the optimal (i.e., unimprovable) multigrid convergence rate pertinent to the solver. At the same time, contrary to the standard local ABCs, the solution accuracy provided by the global ABCs deteriorates very slightly or does not deteriorate at all when the computational domain shrinks, which clearly translates into substantial savings of computer resources.

Keywords: Factorizable scheme; Pressure-Poisson formulation; Multigrid methods; Compressible flow; Incompressible flow; Conformal mapping; Fourier transform; Mode selection; Conservation on the grid; Optimal convergence rate; Exact solution; Error profiles

☆ This research was supported by the National Aeronautics and Space Administration under NASA contract no. NAS1-97046 while the second and third authors were in residence at ICASE, NASA Langley Research Center, Hampton, VA 23681-2199, USA. The work of the third author was supported by Director's Discretionary Fund, NASA Langley Research Center, Hampton, VA 23681-2199.

* Corresponding author. Present address: Department of Mathematics, North Carolina State University, Box 8205, Raleigh, NC 27695, USA. Tel.: +1-919-515-1877; fax: +1-919-515-3798.

E-mail addresses: t.w.roberts@larc.nasa.gov (T.W. Roberts), sidilkov@icase.edu (D. Sidilkover), tsynkov@math.ncsu.edu (S.V. Tsynkov).

URLs: http://www.icase.edu/∼sidilkov, www.math.ncsu.edu/∼stsynkov.

0045-7930/02/$ - see front matter
PII: S0045-7930(01)00045-7

1. Introduction

The subject of this paper is development of the joint formulation, combined implementation, and subsequent performance assessment for the exact nonlocal far-field artificial boundary conditions (ABCs) coupled with the new generation of multigrid flow solvers based on factorizable schemes for the equations of hydrodynamics. Both methodologies have independently proven efficient and promising for the numerical solution of different flow problems and thus it appears natural to try and analyze their performance if combined with one another. Accordingly, we organize the material as follows. First, we briefly review relevant results in the two aforementioned independent areas: Flow solvers and ABCs, and then formulate the motivation and objectives for the current study. Next follows the core of the paper – description of the algorithm and the set of numerical experiments. Finally, we discuss the results that we have obtained, as well as possible extensions for the future.

1.1. Background on the scheme

To emphasize the advantages of the new generation of flow solvers that emerge nowadays, we first briefly review the history of the development of the numerical methods for compressible flow computations.

The full-potential equation is one of the simplest mathematical models describing the compressible fluid flow phenomena. Active research on numerical methods for solving this equation has begun in the early 70s with the work of Murman and Cole [1]. Numerical schemes were developed for two- and three-dimensional cases. Some research has also been done on applying the multigrid methods as a means to accelerate the convergence to steady-state.

The Euler equations constitute a more general model for the fluid flow since they account for the advection of vorticity and entropy as well. The first rather efficient method for the steady-state computations using Euler's equations was developed in early 80s by Jameson and coauthors [2,3]; it still remains (with some modifications) widely used in modern computational practice. However, there was no obvious connection between this new Euler solver and the previously used full-potential solvers. The research on the full-potential solvers was effectively abandoned in its infancy in favor of the solvers for the Euler equations.

On the other hand, it is becoming increasingly clear nowadays that the methods currently used for the steady compressible Euler (and Navier–Stokes) computations have severe limitations in terms of both computational efficacy and robustness.

A major difficulty for the numerical treatment of compressible flow is the possible presence of shocks in the solution. It is well known that a scheme, which is both second order accurate and avoids undershoots and overshoots near discontinuities (which may trigger nonlinear instability), has to be nonlinear. Such a scheme has to incorporate the so-called high-resolution mechanism, i.e., a smoothness monitor, that is usually implemented in the form of a flux limiter. Initially, the schemes of this type were developed for one-dimensional case. Then, they were extended to multiple dimensions using a dimension-by-dimension approach. However, these straightforward multi-dimensional extensions of high-resolution schemes have proven ineffective when applied for calculating the steady-state aerodynamic solutions, which are of great interest for applications. It

turns out that the standard multi-dimensional high-resolution discretizations (obtained by a dimension-by-dimension extension) suffer from the following deficiency: The contribution of the high-frequency error components to the residuals of the discrete equations is very small, which translates into the poor stability characteristics of the steady-state discretization. This makes the construction of a good relaxation scheme, in particular, smoother for a multigrid procedure, inherently difficult, if possible at all. For example, Spekreijse [4] had observed that the Gauss–Seidel relaxation was unstable when implemented along with such schemes. Thus, the multigrid methods based on the Gauss–Seidel relaxation could not be used to accelerate the convergence to steady-state. Instead, the multigrid solvers designed for routine use had to resort to a defect-correction technique or multistage Runge–Kutta relaxation, and as such their efficiency was relatively poor.

A genuinely multi-dimensional advection scheme was constructed in Refs. [5,6]. The scheme was named "genuinely multi-dimensional" since it imitates well the anisotropy of the advection phenomena in two dimensions: The artificial dissipation is added only along the streamline, while the high-resolution mechanism affects significantly the cross-flow direction only. A key feature of this scheme is its two-dimensional limiter, i.e., the limiter-function of an argument that is the ratio of divided differences in two different coordinate directions. The scheme was formulated in the control-volume context for Cartesian grids and relied on the compact 9-point-box stencil. The fundamental advantage of this approach is that the two-dimensional high-resolution mechanism does not damage the stability properties of the steady-state discretization.

Generalization of these ideas to the systems of equations was not straightforward and took substantial time and effort. A generalization of this type that yields a robust scheme for the Euler equations, which is suitable for the computations of a wide range of flow regimes, was presented in Ref. [7]. Later it was described in more detail, including the implications for multigrid and three-dimensional extensions, see Refs. [8,9]. The key idea was not to try and directly apply the scalar advection scheme to the case of systems, but rather start from the scratch and use for the systems the same strategy that was employed to construct the scalar scheme. The resulting scheme for the Euler equations was shown to generate a very good quality solutions for subsonic, transonic, and supersonic regimes. A manifestation of "the genuine multi-dimensionality" of this scheme was rotationally-invariant form of its artificial dissipation.

As in the scalar case, the fundamental advantage of approach [7–9] is that its high-resolution mechanism does not damage the steady-state stability properties of the scheme. Similarly to the scalar case, it was demonstrated in Refs. [8,9] that the Gauss–Seidel relaxation is stable when applied directly to the resulting high-resolution discretization of the hyperbolic systems. This yields a very simple, efficient and robust multigrid solver for the compressible Euler equations suitable for the entire range of flow regimes.

Besides the aforementioned difficulties in the iterative solution of the steady-state flow equations that originate from the poor sensitivity of the residuals to the high-frequency error content, and that have been largely overcome by introducing genuinely multi-dimensional schemes, multigrid iterative solvers are prone to deficiencies of a different nature that can hamper their performance even if a good smoother is available. As outlined in Ref. [10], for the advection dominated problems the coarse grid provides only a fraction of the needed correction for certain

error components. Unlike the previous frequency-based description, this time the "problematic" contributions to the error are the so-called characteristic components, see Ref. [10] (frequency-wise, they are typically mid-range). On the other hand, it is well known that the steady Euler equations can be factored into the advection and full-potential parts; the latter is of either elliptic or hyperbolic type depending on the flow regime (subsonic or supersonic, respectively). The aforementioned difficulty (insufficient coarse-grid corrections for characteristic error components) can be avoided (see Ref. [10]) by constructing a solver that distinguishes between the different factors of the system and treats each one appropriately. In the subsonic case, for instance, the advection factor can be treated by marching and the elliptic factor – by multigrid. The efficiency of such an algorithm will be essentially the same as that of a multigrid solver applied to the elliptic part only. Such algorithms are referred to as "essentially optimal". An approach to separating the co-factors – the so-called distributive Gauss–Seidel relaxation – was proposed in Ref. [10]. It was demonstrated in Ref. [11] that using this approach one can obtain an essentially optimal multigrid efficiency for a staggered-grid discretization of the incompressible Navier–Stokes equations; a similar observation was made earlier in Ref. [12].

Another way (alternative to the distributive Gauss–Seidel relaxation) toward exploiting the elliptic/hyperbolic distinction in the governing equations and thus achieving the optimal multigrid efficiency is based on the well-known pressure formulation of the Euler equations, which also amounts to the factorization of the system into the elliptic and advection parts. A particular formulation of the scheme and the corresponding multigrid algorithm that employ this idea was proposed in Ref. [13]. This approach was further generalized in Ref. [14]; work [14] also contains an extensive set of numerical computations and more detail regarding the implementation of the scheme. The main advantage of this approach is its simplicity, it can also be classified as Weighted Gauss–Seidel relaxation [10]. Subsequent work in this direction is presented in Refs. [15,16]. The limitation of this approach, however, is that it is not clear as of yet whether or not it can be generalized to the case of viscous compressible flows.

It, however, turns out, see Ref. [17], that the idea of factorization that has successfully led to the construction of essentially optimal multigrid solvers in Refs. [10–16] cannot be applied to an important class of schemes that is routinely used for compressible flow computations – the shock-capturing schemes of all types, including the original formulation of genuinely multi-dimensional scheme, see Refs. [7–9]. As these schemes possess a collection of features that cannot be either compromised or traded for in computational practice, primarily the mechanism for handling discontinuous solutions, there is a need for discretization that would rather add the capability of factoring the governing PDEs to the existing properties of the scheme. As has been pointed out in Ref. [17], there is a certain freedom in the way how the multi-dimensional corrections are built for genuinely multi-dimensional schemes [7,8]. These extra freedom can be used to make the resulting scheme also factorizable, i.e., make it capable of reflecting the mixed nature of the governing PDEs. This means that the co-factors of the different type can be distinguished directly at the discrete level (while still keeping the multi-dimensional shock-capturing property). This, in turn, facilitates the construction of an optimally efficient multigrid solver through the design of a special distributive relaxation. The scheme of this type was described in Ref. [18] with the emphasis on the subsonic case. The construction was later extended to the case of three spatial dimensions [19] and generalized coordinates [20]. Extending the approach to the transonic and supersonic regimes is underway.

1.2. Background on the artificial boundary conditions

ABCs furnish a widely used approach for the numerical treatment of boundary-value problems initially formulated on unbounded domains. These boundary conditions are typically set at the external boundary of a finite computational domain once the latter is obtained from the original unbounded domain by means of truncation. Implementation of the ABCs completes the "truncated problem" and therefore, makes it available for solution on the computer. Different authors have repeatedly shown both theoretically and experimentally that the overall accuracy and performance of numerical algorithms, as well as interpretation of the results, strongly depend on the proper treatment of external artificial boundaries.

The choice of the ABCs is typically not unique. Clearly, the minimal necessary requirement of the ABCs is to ensure the solvability of the truncated problem. However, meeting this requirement only does not guarantee that the solution found inside the computational domain will be anywhere close to the corresponding fragment of the solution to the original (infinite-domain) problem. Therefore, we must additionally require that the two solutions be in a certain sense close to one another on the truncated domain. Ideally, these two solutions coincide, which corresponds to the so-called exact ABCs.

It turns out that in most cases, the exact ABCs are nonlocal, for steady-state problems in space and for time-dependent problems also in time. Besides, many methodologies for obtaining exact ABCs lack geometric universality as they rely on integral transforms along the boundary and the separation of variables. In practical computing, the aforementioned nonlocality of the exact ABCs is often translated into cumbersomeness and high computational cost. Thus, along with the accompanying geometric restrictions, it may be regarded as a serious limitation. The alternative is provided by various approximate local methods, which typically meet the other usual requirements of the ABCs besides minimization of the error associated with the domain truncation. These other requirements are low computational cost, geometric universality, and implementation without difficulties. Still, the basic trend in terms of accuracy remains the following: Higher accuracy for the boundary procedure requires more of the nonlocal nature of exact ABCs to be somehow taken into account.

In fact, almost any numerical algorithm for setting the ABCs can be thought of as a compromise between the two foregoing groups of requirements that in a certain sense contradict one another. Shifting the balance towards locality and practical efficacy often implies insufficient accuracy; shifting it to the other end, towards highly accurate nonlocal techniques, may often yield cumbersome and all but impractical algorithms. It is not surprising, therefore, that the treatment of external boundaries in modern production computations typically follows the first, local, path. In computational fluid dynamics (CFD), for example, only a few ABCs' methodologies out of the wide variety proposed to date can be regarded as commonly used tools. All of them are either based on essential model simplifications, e.g., local quasi-one-dimensional treatment in the vicinity of the artificial boundary, or obtained as a localization of some nonlocal ABCs. To meet the overall accuracy requirements when using such simple boundary procedures, one often has to use excessively large computational domains.

An indepth review of different ABCs' methodologies that have been published in the literature over the recent years is available in the paper by Tsynkov [21]. Besides the general review, in this paper we focus on the group of approaches associated with the generalized potentials of

Calderon's type and the difference potentials method (DPM) by Ryaben'kii [22–24]. The application of the DPM provides a new and very powerful vehicle for developing ABCs in different settings. In the framework of the DPM, the boundary conditions are obtained using the equivalent boundary parameterization of the entire variety of exterior solutions; the latter parameterization is built with the help of the so-called generalized Calderon's boundary projections. The DPM-based boundary conditions are usually global. However, when applied, e.g., to solving the steady-state external problems in CFD, they combine the advantages relevant to both global and local methods. In other words, the principal gain from using the DPM is that the method allows one to simultaneously meet the high accuracy standards of the ABCs and the requirements of geometric universality and easiness in implementation. In addition to the review [21], there are original publications on the DPM-based ABCs, we mention here only those closely related to the steady-state compressible viscous aerodynamics, see Refs. [25–33].

The DPM-based ABCs have been implemented along with the NASA-developed multigrid flow solvers in both two and three space dimensions. The investigated flow regimes range from the very low (incompressible limit) to transonic speeds, include different geometries, laminar and turbulent cases, and sometimes, relatively complex flow phenomena, like shock-induced separation and propulsive jets. Compared to the standard local boundary conditions, the DPM-based ABCs provide for much better accuracy and substantially smaller computational domains, significantly faster multigrid convergence [32], and improved robustness of the overall numerical procedure. We particularly emphasize the improved combined performance of global ABCs and multigrid flow solvers as similar behavior has also been observed by other authors [34–38].

In fact, the effect of convergence acceleration when the multigrid algorithm is supplemented by global ABCs [32] was a part of the reason for conducting the current study. Of course, there are significant differences. In our previous work we have used production flow solvers that by themselves have room for improving the performance, at least from the theoretical standpoint. In this work, we use the solver that has already been optimized for performance and thus its convergence rate cannot be improved any further. Therefore, we primarily aim at demonstrating the possibility to significantly reduce the size of the computational domain (and consequently, the grid dimension) while maintaining the solution accuracy, as well as optimal multigrid convergence rate.

1.3. Motivation for the current study

As outlined above, the new factorizable schemes and corresponding multigrid solvers, as well as global DPM-based ABCs, have independently demonstrated performance superior to that of the standard methodologies in various settings. Besides, in many cases the application of global ABCs has helped to speed up the multigrid convergence. Therefore, it seems most natural to try and combine the two techniques – factorizable discretizations with advanced multigrid and global ABCs – with the hope of obtaining a joint methodology that would on one hand be capable of producing accurate flow solutions on domains of substantially reduced size (compared to what the standard methods allow, see, e.g., Refs. [26,31]) and on the other hand, will not hamper the unimprovable multigrid convergence rate displayed by the new type of solvers [14–16].

1.4. Specific objective

Using the simplest existing versions of both the factorizable scheme and nonlocal boundary conditions as a testing ground, we intend to thoroughly work out all the details of merging the two methodologies (from theoretical issues to implementation) and then experimentally study the overall performance for a series of simple problems that allow for a direct comparison with the exact solution. We emphasize that "the simplest existing versions" does not always mean the latest most universal and advanced ones, but rather those that have been tested and that most easily lend themselves to the analysis by analytical means. Specifically, we employ the so-called pressure-Poisson formulation of the factorizable scheme [14–16] for calculating the two-dimensional inviscid incompressible fluid flow around an airfoil. Analytical solutions for such flows are readily available through the use of the conformal mapping technique. The global exact ABCs are also constructed semi-analytically by means of the conformal mapping and Fourier transform along the boundary, with no explicit use of the DPM. The DPM itself will be used at a later stage, when the boundary conditions of the same quality are required for more complex settings.

2. Description of the algorithm

2.1. Discretization of the equations and multigrid algorithm

The algorithm used here is based on a special formulation of the flow equations that involves the so-called pressure-Poisson equation (PPE). The initial version of the algorithm was presented in Ref. [13]. The PPE was derived on the differential level and then discretized. So were the corresponding boundary conditions. It was realized later that deriving the discrete PPE directly can simplify greatly the treatment of the boundary conditions and also introduce some desirable features into the scheme (like a certain conservation property that appeared to be crucial for the purpose of the current work, see Section 2.2.1). This algorithm is described in detail for both unstructured triangular and structured quadrilateral grids in Ref. [15]. Computational results obtained with this algorithm have been presented previously in Refs. [14,16]. In the current work, only structured grids have been used. Since some features of the discretization appeared to be critical for the purpose of this work, namely, constructing the global ABCs that allow to maintain the optimal convergence rates of the algorithm, we shall describe the discretization scheme and the algorithm in detail. The discretization is based on the incompressible Euler equations in primitive variables:

$$u\frac{\partial u}{\partial x}+v\frac{\partial u}{\partial y}+\frac{\partial p}{\partial x}=0,$$

$$u\frac{\partial v}{\partial x}+v\frac{\partial v}{\partial y}+\frac{\partial p}{\partial y}=0,$$

$$\frac{\partial u}{\partial x}+\frac{\partial v}{\partial y}=0,$$

where u and v are Cartesian components of the velocity vector $\boldsymbol{u}$ in the x- and y-directions, respectively, and p is the pressure. The density is taken to be one. The Euler equations can be written in the vector form as follows:

$$(\boldsymbol{u}\cdot\operatorname{grad})\boldsymbol{u}+\operatorname{grad}p=0, \tag{2.1a}$$

$$\operatorname{div}\boldsymbol{u}=0. \tag{2.1b}$$

We shall now derive the PPE formulation of the equations. We subtract from the momentum equation (2.1a) the velocity vector times the continuity equation (2.1b) and apply the divergence operator to the result:

$$\operatorname{div}(\operatorname{grad}p+(\boldsymbol{u}\cdot\operatorname{grad})\boldsymbol{u}-\boldsymbol{u}\operatorname{div}\boldsymbol{u})=0.$$

The previous equation obviously reduces to

$$\Delta p=f\equiv-\operatorname{div}((\boldsymbol{u}\cdot\operatorname{grad})\boldsymbol{u}-\boldsymbol{u}\operatorname{div}\boldsymbol{u}). \tag{2.2}$$

The PPE formulation of the Euler equations is given by replacing the continuity equation (2.1b) by Eq. (2.2), i.e., by using the systems (2.1a) and (2.2) instead of systems (2.1a) and (2.1b); this replacement is obviously equivalent.

The reason for introducing the new PPE formulation is that once we formally consider the transport coefficients in the momentum equation constant, i.e., use the equation

$$(\boldsymbol{a}\cdot\operatorname{grad})\boldsymbol{u}+\operatorname{grad}p=0, \tag{2.3}$$

where $\boldsymbol{a}=\text{const}$, instead of Eq. (2.1a), then Eq. (2.2) becomes a Laplace equation

$$\Delta p=-\operatorname{div}((\boldsymbol{a}\cdot\operatorname{grad})\boldsymbol{u}-\boldsymbol{a}\operatorname{div}\boldsymbol{u})\equiv 0 \tag{2.4}$$

and decouples from the rest of the system. The momentum equation (2.3) can be looked at as a standard advection equation with known forcing function (pressure gradient). We emphasize that in this constant-coefficient case the right-hand side of Eq. (2.4), i.e., the term $-\operatorname{div}((\boldsymbol{a}\cdot\operatorname{grad})\boldsymbol{u}-\boldsymbol{a}\operatorname{div}\boldsymbol{u})$, is equal to zero no matter what the actual value of $\operatorname{div}\boldsymbol{u}$ is. This property is crucial for solving discretizations because on the discrete level the value of $\operatorname{div}\boldsymbol{u}$ is typically of the order of truncation error and not exactly equal to zero; moreover, when solving a discretization by an iterative scheme, initially the value of $\operatorname{div}\boldsymbol{u}$ may simply be far away from zero.

Note that in the general nonlinear case, for smooth slowly varying velocity fields $\boldsymbol{u}$ (in contradistinction to constant $\boldsymbol{a}$), the terms on the right-hand side of Eq. (2.2) can still be considered *subprincipal* (see Ref. [10]) compared to the Laplacian. To illustrate this concept, it is convenient to rewrite Eq. (2.2) as follows:

$$\Delta p=2\left(\frac{\partial u}{\partial x}\frac{\partial v}{\partial y}-\frac{\partial u}{\partial y}\frac{\partial v}{\partial x}\right). \tag{2.5}$$

We qualitatively characterize the velocity field $\boldsymbol{u}=(u,v)$ as slowly varying if for an order h increment in the values of the coordinates, the corresponding increment of the velocity will also be $\mathcal{O}(h)$. (When discretizing the equations later on, h will have the meaning of the grid size.) In this case, the right-hand side of Eq. (2.5) will obviously be $\mathcal{O}(1)$, whereas the left-hand side, i.e., the Laplacian, can be as large as $\mathcal{O}(h^{-1})$ (if we assume similar qualitative behavior of the pressure field). In other words, a given increment in the data results in a much smaller change in the value

of the right-hand side of Eq. (2.5) than that of the Laplacian. Therefore, the right-hand of Eq. (2.5), and consequently, that of Eq. (2.2), introduces only a weak coupling between the pressure equation and the rest of the system. As such, Eq. (2.2) can be considered effectively decoupled from the other equations for the purpose of constructing the relaxation procedure.

We shall now discuss the issue of the boundary conditions for the pressure. The order of the PPE systems (2.1a) and (2.2) is higher (by one) than that of the original systems (2.1a) and (2.1b). Therefore, to ensure the well-posedness of the boundary-value problem, an extra boundary condition for the pressure is required. However, the new problem should still be equivalent to the original one. This implies that this additional boundary condition needs to be derived from the boundary conditions specified for the original problem and, possibly, differential equations of the original system.

Consider a domain Ω with the boundary $\partial\Omega$. Integrating Eq. (2.2) over Ω and applying Gauss' theorem, we obtain

$$\int\int_{\Omega} \operatorname{div}(\operatorname{grad} p + (\boldsymbol{u}\cdot\operatorname{grad})\boldsymbol{u} - \boldsymbol{u}\operatorname{div}\boldsymbol{u})\,\mathrm{d}x\,\mathrm{d}y = \oint_{\partial\Omega} (\operatorname{grad} p + (\boldsymbol{u}\cdot\operatorname{grad})\boldsymbol{u} - \boldsymbol{u}\operatorname{div}\boldsymbol{u})_{\boldsymbol{n}}\,\mathrm{d}s = 0, \tag{2.6}$$

where $\boldsymbol{n}$ is a unit vector normal to the boundary and s is the arc length of $\partial\Omega$. A sufficient condition for equality (2.6) to hold is that at the every point $(x, y) \in \partial\Omega$ the following is true:

$$(\operatorname{grad} p + (\boldsymbol{u}\cdot\operatorname{grad})\boldsymbol{u} - \boldsymbol{u}\operatorname{div}\boldsymbol{u})_{\boldsymbol{n}} = 0. \tag{2.7}$$

We emphasize that as we essentially require in Eq. (2.7) that the overall normal flux be zero at every point on $\partial\Omega$, then we do not need to distinguish ahead of time between the outward and inward normals. In fact, it will be convenient to assume that the normal is always directed toward the center of curvature of $\partial\Omega$, this will allow us to use the Frenet formulae (see below).

Introducing a local orthonormal coordinate frame $(\boldsymbol{n}, \boldsymbol{s})$, where $\boldsymbol{s}$ is a unit vector tangent to $\partial\Omega$, and the corresponding components u_n and u_s of the velocity vector, we can rewrite Eq. (2.7) as follows

$$\frac{\partial p}{\partial \boldsymbol{n}} = -((\boldsymbol{u}\cdot\operatorname{grad})\boldsymbol{u})_{\boldsymbol{n}} + u_{\boldsymbol{n}}\operatorname{div}\boldsymbol{u} = (\boldsymbol{u}\cdot(\boldsymbol{u}\cdot\operatorname{grad})\boldsymbol{n}) + u_{\boldsymbol{n}}\operatorname{div}\boldsymbol{u}. \tag{2.8}$$

Relation (2.8) specifies a general Neumann-type boundary condition for the pressure. If, for example, a particular portion of the boundary under consideration $\partial\Omega'$ is a solid wall, then from the so-called tangency boundary condition for velocity: $\boldsymbol{u}_{\boldsymbol{n}}|_{\partial\Omega'} = 0$, we obtain

$$\frac{\partial p}{\partial \boldsymbol{n}} = (\boldsymbol{u}\cdot(\boldsymbol{u}\cdot\operatorname{grad})\boldsymbol{n}) = u_s((\boldsymbol{u}\cdot\operatorname{grad})\boldsymbol{n})_{\boldsymbol{s}} = u_s^2\frac{\partial \boldsymbol{n}}{\partial \boldsymbol{s}} = -\frac{|\boldsymbol{u}|^2}{\mathscr{R}},$$

where $\mathscr{R} = \mathscr{R}(s)$ is the curvature radius of $\partial\Omega'$. Note, to obtain the last equality in the previous chain we have used the Frenet formulae for plane curves. Clearly, the physical interpretation of the boundary condition

$$\frac{\partial p}{\partial \boldsymbol{n}} = -\frac{|\boldsymbol{u}|^2}{\mathscr{R}} \tag{2.9}$$

is that the normal acceleration of the fluid particles moving tangentially to the wall is directed along the normal $\boldsymbol{n}$, i.e., toward the center of curvature, and equal to the local, i.e., instantaneous, centripetal acceleration. This is because the momentum equation projected onto the normal direction would read that the acceleration of the fluid particles is equal to the minus normal pressure gradient. For a straight wall, boundary condition (2.9) obviously reduces to the zero Neumann boundary condition for the pressure:

$$\frac{\partial p}{\partial \boldsymbol{n}} = 0.$$

Let us now turn to building the discrete scheme. The momentum equations are discretized using a standard first-order upwind-difference approximation to the advection operator and a second-order central-difference approximation to the pressure gradient. To prevent the resulting discretization from degeneration near stagnation points or across streamlines aligned with the grid, a regularizing artificial dissipation term is used. Considering the term $u(\partial u/\partial x)$ in the x-momentum equation, the difference operator is

$$u\frac{\partial^h u}{\partial x} = \frac{1}{2h}(u_{m+1/2,j} - v_{m+1/2,j})(u_{m+1,j} - u_{m,j}) + \frac{1}{2h}(u_{m-1/2,j} + v_{m-1/2,j})(u_{m,j} - u_{m-1,j}),$$

where the superscript h denotes the discrete approximation to the corresponding differential operator, the quantities $u_{m\pm1/2,j}$ are average velocity components given by

$$u_{m+1/2,j} = \frac{1}{2}(u_{m+1,j} + u_{m,j}), \qquad u_{m-1/2,j} = \frac{1}{2}(u_{m,j} + u_{m-1,j}),$$

and $v_{m\pm1/2,j}$ are artificial viscosity coefficients. Analogous expressions can be written for other operators: $v(\partial^h u/\partial y)$, $u(\partial^h v/\partial x)$, and $v(\partial^h v/\partial y)$. The artificial viscosity coefficients $v_{m\pm1/2,j}$ are defined as

$$v_{m\pm1/2,j} = \max\left(\mu\Delta u_{m\pm1/2,j}, \left|u_{m\pm1/2,j}\right|\right),$$

where

$$\Delta u_{m+1/2,j} = (u_{m+1,j} - u_{m,j}), \qquad \Delta u_{m-1/2,j} = (u_{m,j} - u_{m-1,j}),$$

and $\mu \geqslant 1/2$ is an adjustable coefficient, taken to be 0.7 in the current work. This form of the artificial dissipation was presented in Ref. [16].

The discretization of the PPE is based directly on the integral formula (2.6), where the domain Ω is taken to be the control volume $A_{m,j}$ with the boundary $\partial A_{m,j}$ (see Fig. 1):

$$\oint_{\partial A_{m,j}} (\operatorname{grad} p + (\boldsymbol{u}\cdot\operatorname{grad})\boldsymbol{u} - \boldsymbol{u}\operatorname{div}\boldsymbol{u})_{\boldsymbol{n}}\,\mathrm{d}s = 0. \tag{2.10}$$

Breaking the boundary of the control volume $\partial A_{m,j}$ into four parts: "south," "north," "east," and "west" faces, we can rewrite Eq. (2.10) in the following form:

$$h[(F_{m+1/2,j} - F_{m-1/2,j}) + (G_{m,j+1/2} - G_{m,j-1/2})] = 0,$$

where h is the mesh size, $F_{m\pm1/2,j}$ are the east and west fluxes, and $G_{m,j\pm1/2}$ are the north and south fluxes through the faces of the control volume $A_{m,j}$. The fluxes, in their own turn, are evaluated using the midpoint quadrature:

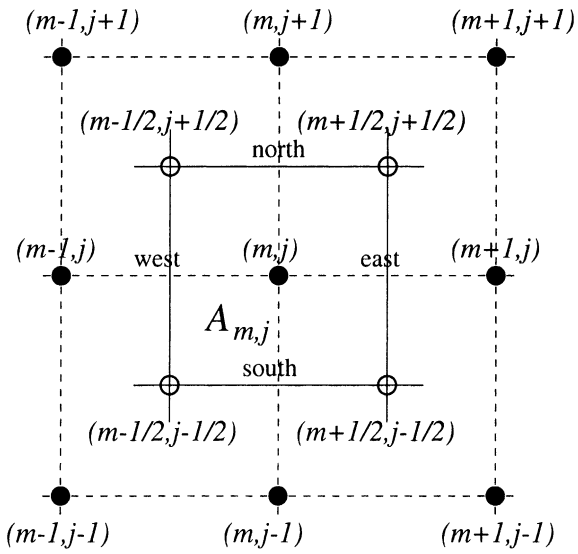

Fig. 1. Computational grid segment and a control volume.

$$
\begin{aligned}
F_{m-1/2,j} &= h[(p_{m,j} - p_{m-1,j}) + v_{m-1/2,j}(u_{m-1/2,j+1/2} - u_{m-1/2,j-1/2}) \\
&\quad - u_{m-1/2,j}(v_{m-1/2,j+1/2} - v_{m-1/2,j-1/2})], \\
G_{m,j-1/2} &= h[(p_{m,j} - p_{m,j-1}) + u_{m,j-1/2}(u_{m+1/2,j-1/2} - u_{m-1/2,j-1/2}) \\
&\quad - v_{m,j-1/2}(v_{m+1/2,j-1/2} - v_{m-1/2,j-1/2})],
\end{aligned}
$$

where the quantities with fractional indices are obtained using either linear or bilinear interpolation:

$$
\begin{aligned}
u_{m-1/2,j} &= (u_{m,j} + u_{m-1,j})/2, \\
u_{m-1/2,j-1/2} &= (u_{m,j} + u_{m-1,j} + u_{m,j-1} + u_{m-1,j-1})/4.
\end{aligned}
$$

The fluxes $F_{m+1/2,j}$ and $G_{m,j+1/2}$ are evaluated similarly.

We now describe the derivation of the discrete PPE at a boundary point $(m,0)$ (see Fig. 2), assuming that no boundary condition on the pressure is prescribed there ahead of time. As in the continuous case, the discrete boundary condition for the pressure will follow from the existing physical boundary conditions and the discrete equations of the finite-difference scheme that we build.

We rewrite equality (2.6) considering the control volume $B_{m,0}$ as the domain shown in Fig. 2

$$
\oint_{\partial B_{m,0}} (\operatorname{grad} p + (\boldsymbol{u}\cdot\operatorname{grad})\boldsymbol{u} - \boldsymbol{u}\operatorname{div}\boldsymbol{u})_{\boldsymbol{n}}\,\mathrm{d}s = 0. \tag{2.11}
$$

Again, as in the case of an internal control volume, we break the integral (2.11) into four parts – fluxes through the four faces of the control volume $B_{m,0}$, and approximate each one of them using the numerical quadrature

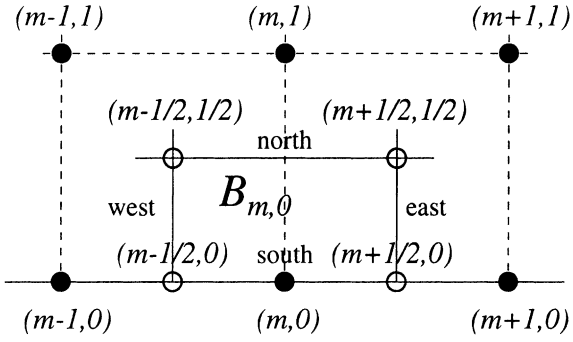

Fig. 2. Boundary control volume.

$$\frac{h}{2}(F_{m+1/2,0} - F_{m-1/2,0}) + h(G_{m,1/2} - G_{m,0}) = 0. \tag{2.12}$$

However, as the "south" face represents now a solid wall, we set the corresponding flux to zero:

$$G_{m,0} = 0. \tag{2.13}$$

This implies (see Eq. (2.7)) imposing the appropriate Neumann boundary condition on the pressure

$$h\frac{\partial^h p}{\partial \boldsymbol{n}} = -u_{m,0}(v_{m+1/2,0} - v_{m-1/2,0}) + v_{m,0}(u_{m+1/2,0} - u_{m-1/2,0}). \tag{2.14}$$

Expression (2.14) can obviously be interpreted as a finite-difference approximation of the equation

$$\frac{\partial p}{\partial y} + u\frac{\partial v}{\partial x} - v\frac{\partial u}{\partial x} = 0,$$

which is a specific version of Eq. (2.7) for the straight solid wall boundary $y = 0$.

The flux $G_{m,1/2}$ in Eq. (2.12) is defined in the same way as for the internal control volume case. For the west flux we use the following formula:

$$F_{m-1/2,0} = \frac{h}{2}(p_{m,0} - p_{m-1,0}) - u_{m-1/2,0}(v_{m-1/2,1/2} - v_{m-1/2,0}) + v_{m-1/2,0}(u_{m-1/2,1/2} - u_{m-1/2,0}),$$

and the east flux $F_{m+1/2,0}$ is evaluated similarly to the above.

This discretization is extended to the body-fitted grids (generalized coordinates) in the same standard way as any control-volume discretization. Therefore, we do not elaborate on this issue here.

2.2. Construction of the artificial boundary conditions

As follows from the previous section, there are three flow quantities to be determined throughout the computation – pressure p and two-velocity components u and v. External boundary condition (i.e., closing mechanism for the discretized equations) will be needed for each of these three quantities. As the exact solution for the problem under study (incompressible inviscid airfoil flow) is known, we, for methodological purposes, will consider different computa-

tional strategies. First, we will be solving for the pressure only while keeping the velocity field on the grid as prescribed by the exact solution. Next, we will be solving for all three-flow quantities. In both cases, we will compare the results obtained with the global ABCs against those obtained with the exact boundary conditions of the Dirichlet type (Dirichlet data at the external boundary taken from the exact solution) and on the other hand, against the results obtained with the standard local ABCs. Accordingly, we construct global ABCs separately for the pressure and for velocities. The boundary conditions are obtained using the separation of variables along the boundary. In many respects, this approach for deriving global ABCs can be regarded standard, see Ref. [21]. In the following Section 2.2.1, we outline this approach and also emphasize the somewhat less standard issues related to conservation and solvability.

2.2.1. Pressure artificial boundary conditions

In the pressure-Poisson formulation that we are using, the elliptic factor in the system is the Poisson equation for the pressure

$$\Delta p = f, \tag{2.15}$$

which is to be solved on the infinite domain exterior to the airfoil subject to the condition of boundedness of the solution at infinity and the Neumann boundary condition

$$\left.\frac{\partial p}{\partial \boldsymbol{n}}\right|_{\Gamma} = \psi \tag{2.16}$$

on the airfoil surface Γ. As mentioned in Section 2.1, boundary condition (2.16) is simply a reformulation of the momentum equation in the direction normal to the solid wall, the function ψ represents centripetal acceleration (depends on the tangential velocity), the continuous explicit expression for ψ is given in Eq. (2.9), and the discretization is built as shown in Eq. (2.14). The only difference to be emphasized between boundary condition (2.16) and considerations of Section 2.1, see formula (2.9), is that formerly we have considered the normal $\boldsymbol{n}$ always pointing to the center of curvature of Γ, whereas $\boldsymbol{n}$ in Eq. (2.16) is the normal to Γ with the fixed direction toward the interior of the airfoil (i.e., external normal for the flow domain). Therefore, the sign of the centripetal acceleration in the function ψ will depend on whether the curve Γ is convex or concave at every particular location. Similarly to ψ, the right-hand side f of Eq. (2.15) also depends on the velocities, the explicit expression for f is given in Eq. (2.2). Note, a more general and more recent formulation of the scheme involves the equation for the velocity potential rather than pressure as the elliptic factor. For incompressible flows, this equation is always homogeneous, which, in particular, makes the construction of the ABCs conceptually more straightforward. In the current formulation, as will be seen, taking care of the inhomogeneity f requires special attention. The corresponding experience, however, is going to be useful for the future analysis of the compressible case in a similar framework.

Let us now denote by Ω the unbounded domain on which we are solving Eq. (2.15), then $\Gamma = \partial\Omega$. An obvious necessary condition for solvability of problem (2.15), (2.16) with p bounded at infinity is the equality of the sum of all sources inside the domain Ω to the total flux through its boundary Γ, i.e.,

$$\int\int_{\Omega} f \, \mathrm{d}\Omega = \int_{\Gamma} \psi \, \mathrm{d}\Gamma. \tag{2.17}$$

Next, we map the domain Ω of variable $z = x + \mathrm{i}y \in \mathscr{C}$ (exterior of the airfoil) conformally onto the exterior of the unit disk $\{|\zeta| > 1\,|, \zeta = \xi + \mathrm{i}\eta \in \mathscr{C}\}$. (The mapping is determined uniquely by requiring that $z = \infty \to \zeta = \infty$ and specifying the angle of rotation $\arg \zeta'_z(\infty)$.) The Laplace operator of Eq. (2.15) does not change with the conformal mapping. Consequently, if we introduce polar coordinates (ρ, θ) on the complex plane of variable $\zeta = \xi + \mathrm{i}\eta$, then Eq. (2.15) and boundary condition (2.16) transform into

$$\frac{1}{\rho}\frac{\partial}{\partial\rho}\left(\rho\frac{\partial p}{\partial\rho}\right) + \frac{1}{\rho^2}\frac{\partial^2 p}{\partial\theta^2} = f(\rho,\theta) \tag{2.18}$$

and

$$-\left.\frac{\partial p}{\partial\rho}\right|_{\rho=1} = \psi(\theta), \tag{2.19}$$

respectively. The external artificial boundary on the plane ζ will be a circle of radius R centered at the origin: $\rho = R$. As we will see in Section 3.1, the grid used for the numerical integration of the flow equations is obtained by transforming a polar grid from the plane ζ back to the plane z. This transform maps the circle $\rho = R$ onto the outer coordinate line of the curvilinear boundary-fitted conformal grid built around the airfoil. On the circle $\rho = R$, we need to construct the ABCs that would guarantee that the solution of Eq. (2.18) with boundary condition (2.19) found for $1 \leqslant \rho \leqslant R$ can be smoothly extended beyond $\rho = R$ to the entire infinite domain $\rho \geqslant 1$ so that the extended solution satisfy the same differential equation and wall boundary condition and also be bounded at infinity.

When constructing the ABCs, we will start with considering a particular case of $f(\rho,\theta) \equiv 0$ for $\rho \geqslant R$. The motivation for that is twofold. First, it will always be the case for the new formulation of the scheme for incompressible flows. Second, in many other situations, the right-hand side f, although not exactly zero, decays sufficiently fast in the far field so that by neglecting it outside the computational domain (i.e., outside the artificial boundary) one does not introduce large errors. Experimentally, it is always possible to see whether or not the assumption of homogeneity in the far field is acceptable [26,27,30,31,33].

In general, the case when the governing equations are homogeneous in the far field is central for most ABCs' methodologies, see Ref. [21]. For the particular formulation under study, having built the homogeneous ABCs we will also show how one can explicitly take into account the inhomogeneity f, see Eq. (2.18).

The homogeneous boundary conditions are most easily obtained in the continuous formulation. We Fourier transform Eq. (2.18) in θ and as $f(\rho,\theta) = 0$ for $\rho \geqslant R$, arrive at the following family of ordinary differential equations

$$\frac{1}{\rho}\frac{\mathrm{d}}{\mathrm{d}\rho}\left(\rho\frac{\mathrm{d}\hat{p}_k}{\mathrm{d}\rho}\right) - \frac{k^2}{\rho^2}\hat{p}_k = 0, \quad \rho \geqslant R, \;\; k = 0, \pm1, \pm2, \ldots, \tag{2.20}$$

parameterized by the wavenumber k. For $k \neq 0$, the corresponding homogeneous equation from Eq. (2.20) has two linearly independent solutions: $\hat{p}_k^{(1)} = \rho^{|k|}$ and $\hat{p}_k^{(2)} = \rho^{-|k|}$. Boundedness at in-

finity implies that all modes $\hat{p}_k^{(1)}$ for all $k = \pm 1, \pm 2, \ldots$ should be excluded, which is equivalent to the following countable set of conditions written in terms of the Wronskians:

$$\det \begin{bmatrix} \hat{p}_k & \hat{p}_k^{(2)} \\ \frac{\mathrm{d}\hat{p}_k}{\mathrm{d}\rho} & \frac{\mathrm{d}\hat{p}_k^{(2)}}{\mathrm{d}\rho} \end{bmatrix} = 0, \qquad k = \pm 1, \pm 2, \ldots. \tag{2.21}$$

Conditions (2.21) can, in fact, be imposed at any location ρ, at which Eq. (2.18) is homogeneous; setting Eq. (2.21) at $\rho = R$ immediately yields

$$\left.\frac{\mathrm{d}\hat{p}_k}{\mathrm{d}\rho}\right|_{\rho=R} + \left.\frac{|k|}{R}\hat{p}_k\right|_{\rho=R} = 0, \quad k = \pm 1, \pm 2, \ldots. \tag{2.22a}$$

As concerns $k = 0$, the general solution of the corresponding homogeneous equation from (2.20) is $C_1 + C_2 \ln \rho$. Boundedness at infinity implies $C_2 = 0$, which leads to the following boundary condition

$$\left.\frac{\mathrm{d}\hat{p}_0}{\mathrm{d}\rho}\right|_{\rho=R} = 0, \tag{2.22b}$$

which can also be formally obtained from Eq. (2.22a) by letting $k = 0$. The countable sequence of relations (2.22b) and (2.22a) for $k = 0, \pm 1, \pm 2, \ldots$ constitutes the full set of exact ABCs at the external artificial boundary $\rho = R$. Boundary conditions (2.22) are applicable provided that $f(\rho, \theta) = 0$ for $\rho \geqslant R$. They guarantee that the solution calculated for $\rho \leqslant R$ can be smoothly and uniquely complemented to the entire infinite domain so that the complement solve Eq. (2.18) and be bounded at infinity.

Note, after the Fourier transform back to the physical space, the ABCs obtained by the separation of variables along the boundary typically become nonlocal (e.g., ABCs (2.22)). Most often, these ABCs (in the physical space) are represented by means of pseudodifferential operators, see Ref. [21]. For the particular case of Eqs. (2.22a) and (2.22b), however, a representation via singular integrals is also available; it was obtained by Lončarić in Ref. [39] and involves the kernel $\ln\left|\sin\frac{\theta}{2}\right|$.

Let us now consider the inhomogeneous case, when, generally speaking, $f(\rho, \theta) \neq 0$ for $\rho \geqslant R$. After the Fourier transform in θ we obtain (cf. Eq. (2.20))

$$\frac{1}{\rho}\frac{\mathrm{d}}{\mathrm{d}\rho}\left(\rho\frac{\mathrm{d}\hat{p}_k}{\mathrm{d}\rho}\right) - \frac{k^2}{\rho^2}\hat{p}_k = \hat{f}_k(\rho), \quad \rho \geqslant 1, \;\; k = 0, \pm 1, \pm 2, \ldots. \tag{2.23}$$

To discuss the solvability issues, we will also need to Fourier transform Eq. (2.19), which yields

$$-\left.\frac{\mathrm{d}\hat{p}_k}{\mathrm{d}\rho}\right|_{\rho=1} = \hat{\psi}_k, \quad k = 0, \pm 1, \pm 2, \ldots. \tag{2.24}$$

We start with the analysis of the case $k = 0$, which differs from the analysis for all other ks. In Fourier space on the new plane ζ, the solvability condition (2.17) obviously transforms into

$$\int_1^{+\infty} \hat{f}_0(\rho)\rho\,\mathrm{d}\rho = -\left.\frac{\mathrm{d}\hat{p}_0}{\mathrm{d}\rho}\right|_{\rho=1} = \hat{\psi}_0. \tag{2.25}$$

We now integrate Eq. (2.23) for $k = 0$ from $\rho = 1$ to $\rho = R$ and obtain:

$$\int_1^R \frac{\mathrm{d}}{\mathrm{d}\rho}\left(\rho\frac{\mathrm{d}\hat{p}_0}{\mathrm{d}\rho}\right)\mathrm{d}\rho = \left.\rho\frac{\mathrm{d}\hat{p}_0}{\mathrm{d}\rho}\right|_{\rho=R} - \left.\frac{\mathrm{d}\hat{p}_0}{\mathrm{d}\rho}\right|_{\rho=1} = \int_1^R \hat{f}_0(\rho)\rho\,\mathrm{d}\rho. \tag{2.26}$$

The combination of formulae (2.25) and (2.26) immediately yields

$$\left.\rho\frac{\mathrm{d}\hat{p}_0}{\mathrm{d}\rho}\right|_{\rho=R} = \int_1^R \hat{f}_0(\rho)\rho\ \mathrm{d}\rho - \hat{\psi}_0. \tag{2.27}$$

Inhomogeneous relation (2.27) will replace homogeneous relation (2.22b) for $k = 0$ in the countable sequence of boundary conditions in Fourier space. Note, if we assume for a moment, as before, that $\hat{f}_0(\rho) = 0$ for $\rho \geqslant R$, then obviously

$$\int_1^R \hat{f}_0(\rho)\rho\ \mathrm{d}\rho = \int_1^{+\infty} \hat{f}_0(\rho)\rho\ \mathrm{d}\rho,$$

and because of Eq. (2.25) the right-hand side of Eq. (2.27) vanishes and condition (2.27) transforms back into (2.22b).

Let us now emphasize a very important circumstance. Specifying Neumann boundary conditions for $k = 0$ both at $\rho = 1$ and $\rho = R$ may, generally speaking, be problematic from the standpoint of solvability. Indeed, in the fully homogeneous case neither of these boundary conditions admits the logarithmic mode and both admit the constant mode. Thus, $\hat{p}_0 = \text{const}$ will solve the homogeneous problem

$$\frac{1}{\rho}\frac{\mathrm{d}}{\mathrm{d}\rho}\left(\rho\frac{\mathrm{d}\hat{p}_0}{\mathrm{d}\rho}\right) = 0, \quad \left.\frac{\mathrm{d}\hat{p}_0}{\mathrm{d}\rho}\right|_{\rho=1} = 0, \qquad \left.\frac{\mathrm{d}\hat{p}_0}{\mathrm{d}\rho}\right|_{\rho=R} = 0.$$

Consequently, the corresponding nonhomogeneous problem will not be solvable for any right-hand side, and in case it is solvable, the solution will not be unique. However, the type of the boundary conditions (Neumann) for $k = 0$ cannot be changed/relaxed because at both $\rho = 1$ and $\rho = R$ these boundary conditions are obtained from the physical considerations. Therefore, some additional solvability conditions are introduced that limit the general admissible scope of the problem data.

For the original infinite-domain problem the solvability condition in the Fourier space is given by relation (2.25). For the truncated problem, it is rewritten in the form Eq. (2.27), and in the homogeneous case it further reduces to Eq. (2.22b). It is very convenient that in the formulation that involves ABCs, the solvability condition (2.27) (or (2.22b)) is not added to the countable family of ABCs in Fourier space for $k = 0, \pm 1 \pm 2, \ldots$, but rather comes naturally as one particular element of this sequence that corresponds to $k = 0$.

Clearly, the homogeneous boundary condition (2.22b) can be interpreted as zero flux through the outer boundary and thus it corroborates the natural physical meaning of the solvability condition. When a non-zero right-hand f side extends beyond $\rho = R$, we replace Eq. (2.22b) with

the nonhomogeneous boundary condition (2.27) to ensure the solvability. The meaning of (2.27) is, of course, the same – it is conservation, and the difference compared to (2.22b) is that now because of a different right-hand side the flux through the outer boundary is no longer zero. It is important that inhomogeneity on the right-hand side of equality (2.27):

$$\int_1^R \hat{f}_0(\rho)\rho\,\mathrm{d}\rho - \hat{\psi}_0 = \int_R^{+\infty} \hat{f}_0(\rho)\rho\;\mathrm{d}\rho$$

cannot be neglected even if $\hat{f}_0(\rho)$ is small for $\rho > R$. As has been mentioned, the latter is often the case, but disregarding the aforementioned inhomogeneity will make this problem unsolvable rather than simply introduce a small error into the boundary conditions and thus into the solution. In many other situations (see, e.g., below) introducing such errors is not dangerous from the standpoint of solvability, and the extent to which the solution may deteriorate as a result can always be estimated aposteriori (see Ref. [21]). In the particular case under study, strict conservation of type (2.27) has to be enforced not only in the continuous framework, but also on the grid; this issue will be discussed later.

For all other modes except $k = 0$, i.e., $k = \pm 1, \pm 2, \ldots$, it is easy to see that the homogeneous problem

$$\frac{1}{\rho}\frac{\mathrm{d}}{\mathrm{d}\rho}\left(\rho\frac{\mathrm{d}\hat{p}_k}{\mathrm{d}\rho}\right) - \frac{k^2}{\rho^2}\hat{p}_k = 0, \qquad \left.\frac{\mathrm{d}\hat{p}_k}{\mathrm{d}\rho}\right|_{\rho=1} = 0, \qquad \left.\frac{\mathrm{d}\hat{p}_k}{\mathrm{d}\rho}\right|_{\rho=R} + \left.\frac{|k|}{R}\hat{p}_k\right|_{\rho=R} = 0,$$

has only trivial solution (indeed, both $\hat{p}_k^{(1)}$ and $\hat{p}_k^{(2)}$ are eliminated by the boundary conditions) and therefore the corresponding nonhomogeneous problem is solvable for any right-hand side (inhomogeneities, i.e., right-hand sides, can be introduced into the boundary conditions themselves as well). Therefore, the situation here is entirely different compared to the case $k = 0$. Namely, boundary conditions (2.22a) are exact when the far field is homogeneous, $f(\rho, \theta) = 0$ for $\rho \geqslant R$. If a far-field inhomogeneity is introduced, its effect can, in principle, be incorporated into these boundary conditions making them nonhomogeneous as well. However, when the far-field inhomogeneity is small it can be neglected, which will not give rise to any solvability concerns for $k \neq 0$, and the corresponding error in the numerical solution will then be estimated by a posteriori numerical checks, see, e.g., Refs. [26,27,30,31,33].

Note, the incorporation of inhomogeneity into the boundary conditions (2.22a), $k \neq 0$, is not going to be as easy as obtaining relation (2.27) instead of Eq. (2.22b). A general "conceptual" recipe for such an incorporation can be found, e.g., in Ref. [23]; but it basically amounts to integrating (essentially, solving) the nonhomogeneous differential equation on the infinite portion of the domain that is being truncated and replaced by the ABCs. This is exactly what we are trying to avoid; besides, it is typically not feasible. Therefore, in the numerical experiments below we study the non-lifting flows so that the entire inhomogeneity of the problem is concentrated on the zeroth Fourier mode $k = 0$ only. This helps us focus on our goal of demonstrating that optimal convergence of the solver can be recovered with global ABCs in the simplest (i.e., ideal) regime.

To derive the ABCs for the finite-difference scheme we follow a procedure similar to the one we used for obtaining the continuous boundary conditions. The grid on the plane ζ is a polar grid uniform in θ and stretched in ρ; when mapped back onto the plane z it yields a curvilinear O-type grid fitted to the airfoil surface. The grid has J cells in the radial direction with the nodes ρ_j,

$j = 0, \ldots, J$, so that $\rho_0 = 1$ and $\rho_j = R$, and M cells in the circumferential direction with the constant grid size $\Delta\theta = 2\pi/M$ and nodes $\theta_m = m\Delta\theta$, $m = 0, \ldots, M$; due to periodicity the angular directions $\theta_0 = 0$ and $\theta_M = 2\pi$ coincide.

A second-order accurate discretization of the PPE that we use is outlined in Section 2.1. It is a finite-volume discretization performed directly on the curvilinear body-fitted grid in the physical plane z. It is easy to check however, that if the exact same finite-volume approach was applied to the polar grid on the model plane ζ, then for Eq. (2.18) it would result in the following natural central-difference discretization:

$$\frac{1}{\rho_j}\frac{1}{\Delta\rho_j}\left(\rho_{j+1/2}\frac{p_{m,j+1}-p_{m,j}}{\Delta\rho_{j+1/2}}-\rho_{j-1/2}\frac{p_{m,j}-p_{m,j-1}}{\Delta\rho_{j-1/2}}\right)+\frac{1}{\rho_j^2}\frac{p_{m+1,j}-2p_{m,j}+p_{m-1,j}}{\Delta\theta^2}=f_{m,j}, \tag{2.28}$$

where $\rho_{j+1/2} = (\rho_{j+1} + \rho_j)/2$, $\rho_{j-1/2} = (\rho_j + \rho_{j-1})/2$, $\Delta\rho_{j+1/2} = \rho_{j+1} - \rho_j$, $\Delta\rho_{j-1/2} = \rho_j - \rho_{j-1}$, and $\Delta\rho_j = (\Delta\rho_{j-1/2} + \Delta\rho_{j+1/2})/2$. Finite-difference equation (2.28) will be used for deriving the discrete counterpart to the nonhomogeneous boundary condition (2.27).

Along with the fully discrete equation (2.28) we will also consider a semi-discrete form of the homogeneous equation in the far field:

$$\frac{1}{\rho}\frac{\mathrm{d}}{\mathrm{d}\rho}\left(\rho\frac{\mathrm{d}p_m}{\mathrm{d}\rho}\right)+\frac{1}{\rho^2}\frac{p_{m+1}-2p_m+p_{m-1}}{\Delta\theta^2}=0, \quad m=0,\ldots,M-1. \tag{2.29}$$

Introducing the direct discrete Fourier transform

$$\hat{p}_k = \frac{1}{M}\sum_{m=0}^{M-1} p_m \mathrm{e}^{-\mathrm{i}km\Delta\theta}, \quad k = -\frac{M}{2}+1,\ldots,\frac{M}{2}, \tag{2.30a}$$

and inverse discrete Fourier transform

$$p_m = \sum_{k=-M/2+1}^{M/2} \hat{p}_k \mathrm{e}^{\mathrm{i}km\Delta\theta}, \quad m = 0,\ldots,M-1, \tag{2.30b}$$

on the grid, we reduce Eq. (2.29) to

$$\frac{1}{\rho}\frac{\mathrm{d}}{\mathrm{d}\rho}\left(\rho\frac{\mathrm{d}\hat{p}_k}{\mathrm{d}\rho}\right)-\frac{\alpha_k^2}{\rho^2}\hat{p}_k=0, \qquad k=-\frac{M}{2}+1,\ldots,\frac{M}{2}, \quad \alpha_k^2=\frac{4}{\Delta\theta^2}\sin^2\frac{k\Delta\theta}{2}. \tag{2.31}$$

For any particular k, Eq. (2.31) looks very much like Eq. (2.20) except that k^2 is replaced by α_k^2. To obtain the boundary conditions, we introduce a row of ghost nodes with $j = J+1$, $\rho_{J+1} = \rho_J + \Delta\rho_{J+1/2} = R + \Delta\rho_{J+1/2}$, and first write down the system of equalities similar to Eq. (2.22a) but at the location $\rho = \rho_{J+1/2} = R + \Delta\rho_{J+1/2}/2$ rather than $\rho = R$ ($k \neq 0$):

$$\left.\frac{\mathrm{d}\hat{p}_k}{\mathrm{d}\rho}\right|_{\rho=\rho_{J+1/2}}+\left.\frac{|\alpha_k|}{\rho_{J+1/2}}\hat{p}_k\right|_{\rho=\rho_{J+1/2}}=0, \quad k=-\frac{M}{2}+1,\ldots,-1,\,1,\ldots,\frac{M}{2}. \tag{2.32}$$

Then we discretize Eq. (2.32) consistently with the central-difference discretization (2.28), which yields

$$\frac{\hat{p}_{k,J+1}-\hat{p}_{k,J}}{\Delta\rho_{J+1/2}}+\frac{|\alpha_k|}{\rho_{J+1/2}}\frac{\hat{p}_{k,J+1}+\hat{p}_{k,J}}{2}=0,\quad k=-\frac{M}{2}+1,\ldots,-1,1,\ldots,\frac{M}{2},\tag{2.33}$$

or

$$\hat{p}_{k,J+1}\left(\frac{|\alpha_k|}{2}+\frac{\rho_{J+1/2}}{\Delta\rho_{J+1/2}}\right)=-\hat{p}_{k,J}\left(\frac{|\alpha_k|}{2}-\frac{\rho_{J+1/2}}{\Delta\rho_{J+1/2}}\right),\quad k=-\frac{M}{2}+1,\ldots,-1,1,\ldots,\frac{M}{2}.\tag{2.34a}$$

The remaining mode $k=0$ is treated separately as before; in the homogeneous case instead of Eq. (2.22b) we have:

$$\frac{\hat{p}_{0,J+1}-\hat{p}_{0,J}}{\Delta\rho_{J+1/2}}=0,$$

or

$$\hat{p}_{0,J+1}=\hat{p}_{0,J}.\tag{2.34b}$$

Note, as in the case of the continuous boundary conditions (2.22b) and (2.22a), relation (2.34b) can also be formally obtained from Eq. (2.34a) by substituting $\alpha_k=0$ for $k=0$. In the physical discrete space we can rewrite the system of equalities (2.34a) and (2.34b) as one matrix relation

$$\boldsymbol{p}_{J+1}=\boldsymbol{F}^{-1}\mathrm{diag}\{\beta_k\}\boldsymbol{F}\boldsymbol{p}_J\equiv\boldsymbol{T}\boldsymbol{p}_J,\tag{2.35}$$

where

$$\beta_k=-\left(\frac{|\alpha_k|}{2}-\frac{\rho_{J+1/2}}{\Delta\rho_{J+1/2}}\right)\cdot\left(\frac{|\alpha_k|}{2}+\frac{\rho_{J+1/2}}{\Delta\rho_{J+1/2}}\right)^{-1}\quad\text{if}\quad k=-\frac{M}{2}+1,\ldots,-1,1,\ldots,\frac{M}{2},\ \beta_0=1,\tag{2.36}$$

$\boldsymbol{p}_J$ and $\boldsymbol{p}_{J+1}$ are the M-component vectors that contain the grid values of p for the last row of nodes $j=J$ and the row of ghost nodes $j=J+1$, respectively, and $\boldsymbol{F}^{-1}$ and $\boldsymbol{F}$ are $M\times M$ matrices that denote the inverse (2.30b) and direct (2.30a) discrete Fourier transforms, respectively.

Let us point out some easy-to-see properties of the matrix $\boldsymbol{T}$ of Eq. (2.35). First, this matrix is circulant:

$$\boldsymbol{T}=\begin{bmatrix} t_0 & t_{M-1} & t_{M-2} & \cdots & t_1\\ t_1 & t_0 & t_{M-1} & \cdots & t_2\\ t_2 & t_1 & t_0 & \cdots & t_3\\ \vdots & \vdots & \vdots & \ddots & \vdots\\ t_{M-1} & t_{M-2} & t_{M-3} & \cdots & t_0 \end{bmatrix}.\tag{2.37}$$

This follows immediately from the periodicity in circumferential direction. Moreover, the matrix $\boldsymbol{T}$ is symmetric because $t_j=t_{M-j}$ for $j=1,\ldots,M-1$; these equalities simply reflect the fact that the response to a point source on the circular boundary will be the same in both clockwise and counterclockwise directions. Finally, all eigenvalues β_k of the matrix $\boldsymbol{T}$, see Eq. (2.36), are non-negative and moreover, $0\leqslant\beta_k\leqslant 1$ for $k=-M/2+1,\ldots,M/2$. Indeed, as mentioned in Section 3.1

below, the grids that we actually use for our computations are stretched in the radial direction so that to maintain the cell aspect ratio equal to one throughout the entire domain. This, in fact, means that $\rho_{J+1/2}/\Delta\rho_{J+1/2} = 1/\Delta\theta$, and recalling the definition of α_k, see Eq. (2.31), we conclude that the first expression in brackets in the definition of β_k, see Eq. (2.36), is always non-positive. Thus, $\beta_k \geqslant 0$. The second inequality for the magnitude of β_k follows directly from formula (2.36). The aforementioned properties may be beneficial from the standpoint of multigrid analysis, as well as a certain type of implementation, see Section 2.3. However, it yet remains to be seen whether similar properties can be established for more general cases.

When a far-filed inhomogeneity is present, we need, as has been shown, special treatment for the zeroth Fourier mode $k = 0$. First, we write down the one-dimensional finite-difference equation

$$\frac{1}{\rho_j}\frac{1}{\Delta\rho_j}\left(\rho_{j+1/2}\frac{\hat{p}_{0,j+1}-\hat{p}_{0,j}}{\Delta\rho_{j+1/2}}-\rho_{j-1/2}\frac{\hat{p}_{0,j}-\hat{p}_{0,j-1}}{\Delta\rho_{j-1/2}}\right)=\hat{f}_{0,j}, \tag{2.38}$$

which one can obtain directly from Eq. (2.28), and notice that $\hat{p}_{0,j} = \text{const}$ is a solution to the homogeneous counterpart of Eq. (2.38). The second linearly independent solution to Eq. (2.38) has to grow for large js as on any finite domain it should approximate $\ln\rho$; this second mode is prohibited by boundary condition (2.34b) for the homogeneous case when $\hat{f}_{0,j} = 0$ for $j \geqslant J$. Let us now perform summation by j from $j = 1$ to $j = J$ on both sides of Eq. (2.38), this discrete operation is an analogue of the integration (2.26):

$$\sum_{j=1}^{J}\left(\rho_{j+1/2}\frac{\hat{p}_{0,j+1}-\hat{p}_{0,j}}{\Delta\rho_{j+1/2}}-\rho_{j-1/2}\frac{\hat{p}_{0,j}-\hat{p}_{0,j-1}}{\Delta\rho_{j-1/2}}\right)=\rho_{J+1/2}\frac{\hat{p}_{0,J+1}-\hat{p}_{0,J}}{\Delta\rho_{J+1/2}}-\rho_{1/2}\frac{\hat{p}_{0,1}-\hat{p}_{0,0}}{\Delta\rho_{1/2}}=\sum_{j=1}^{J}\rho_j\Delta\rho_j\hat{f}_{0,j}. \tag{2.39}$$

From Eq. (2.39) we conclude that we need to replace Eq. (2.34b) by the following nonhomogeneous boundary condition:

$$\rho_{J+1/2}\frac{\hat{p}_{0,J+1}-\hat{p}_{0,J}}{\Delta\rho_{J+1/2}}=\sum_{j=1}^{J}\rho_j\Delta\rho_j\hat{f}_{0,j}+\rho_{1/2}\frac{\hat{p}_{0,1}-\hat{p}_{0,0}}{\Delta\rho_{1/2}}, \tag{2.40}$$

which is a discrete counterpart to Eq. (2.27).

Let us now note that $f_{m,j}$ has a rather special structure – it can be represented using the divergence theorem as fluxes through the boundary of a control volume $A_{m,j}$ shown on Fig. 1, see the discussion in Section 2.1. On the polar grid, the area of this control volume is

$$\frac{\pi(\rho_{j+1/2}^2-\rho_{j-1/2}^2)}{M}=\frac{2\pi\rho_j\Delta\rho_j}{M}.$$

Now, applying the divergence theorem, we obtain

$$\frac{2\pi\rho_j\Delta\rho_j}{M}f_{m,j}=\Delta\rho_j(F^f_{m+1/2,j}-F^f_{m-1/2,j})+\left(\frac{2\pi\rho_{j+1/2}}{M}G^f_{m,j+1/2}-\frac{2\pi\rho_{j-1/2}}{M}G^f_{m,j-1/2}\right). \tag{2.41}$$

Notice, unlike in Section 2.1, the fluxes $F^f_{m\pm1/2,j}$ and $G^f_{m,j\pm1/2}$ in Eq. (2.41) have the superscript f; this emphasizes that they take into account only the contribution of the actual right-hand side f

of Eq. (2.2). This means that instead of evaluating integral (2.10) using the control volume approach, we evaluate a similar integral with grad p taken out and thus only the velocity's contribution left.

Calculating now the zeroth Fourier component of $f_{m,j}$, see Eq. (2.30a), and using Eq. (2.41) we obtain

$$\hat{f}_{0,j} = \frac{1}{M}\sum_{m=0}^{M-1} f_{m,j} = \frac{1}{M\rho_j \Delta\rho_j}\left(\rho_{j+1/2}\sum_{m=0}^{M-1} G^f_{m,j+1/2} - \rho_{j-1/2}\sum_{m=0}^{M-1} G^f_{m,j-1/2}\right).$$

Substituting the previous expression into Eq. (2.40) yields

$$\rho_{J+1/2}\frac{\hat{p}_{0,J+1} - \hat{p}_{0,J}}{\Delta\rho_{J+1/2}} = \frac{\rho_{J+1/2}}{M}\sum_{m=0}^{M-1} G^f_{m,J+1/2} - \frac{\rho_{1/2}}{M}\sum_{m=0}^{M-1} G^f_{m,1/2} + \rho_{1/2}\frac{\hat{p}_{0,1} - \hat{p}_{0,0}}{\Delta\rho_{1/2}}. \tag{2.42}$$

Clearly, the discussion in Section 2.1 and more precisely, the requirement (2.13) of zero flux through the boundary that leads to the boundary condition (2.14) on the solid wall, implies that

$$\frac{\rho_{1/2}}{M}\sum_{m=0}^{M-1} G^f_{m,1/2} = \rho_{1/2}\frac{\hat{p}_{0,1} - \hat{p}_{0,0}}{\Delta\rho_{1/2}}.$$

Therefore, we obtain

$$\frac{\hat{p}_{0,J+1} - \hat{p}_{0,J}}{\Delta\rho_{J+1/2}} = \frac{1}{M}\sum_{m=0}^{M-1} G^f_{m,J+1/2}. \tag{2.43}$$

Relation (2.40) and its particular form (2.43) represent the exact conservation on the grid that is required for the solvability of the discrete problem. The inhomogeneity on the zeroth Fourier mode, see Eq. (2.43), can also be included into the boundary condition in the matrix form, which will then read

$$\boldsymbol{p}_{J+1} = \boldsymbol{T}\boldsymbol{p}_J + \frac{\Delta\rho_{J+1/2}}{2\pi\rho_{J+1/2}}\bar{f}_{\cdot,J}, \tag{2.44}$$

where $\bar{f}_{\cdot,J}$ is the total flux due to the forcing term through the outer faces of the control volumes centered at the Jth gridline.

From the standpoint of implementation, boundary conditions (2.35) or (2.44) are matrix-vector relations that connect the values of the solution p on the last row of grid nodes $j = J$ and the row of ghost nodes $j = J + 1$. These boundary conditions are built so that to allow the correct complement of the solution from the finite computational domain to its infinite exterior. As the two problems on the planes z and ζ are obviously equivalent (via the conformal mapping), then the discrete ABCs (2.35) or (2.44) obtained originally for the plane ζ can be used on the plane z with no changes, simply as the equalities connecting the values of the solution on two rows of the grid through matrix-vector multiplication. This property has been fully corroborated experimentally, see Section 3, even so the finite-difference equation for the pressure on the actual body-fitted grid may differ from Eq. (2.28) in the sense that the stencil may contain more than five nodes for those cells that noticeably differ in shape from rectangles.

2.2.2. Artificial boundary conditions for velocities

It is known that for the particular case under study the quantities u and $-v$ satisfy the Cauchy–Riemann equations:

$$\frac{\partial u}{\partial x} = -\frac{\partial v}{\partial y}, \qquad \frac{\partial u}{\partial y} = \frac{\partial v}{\partial x}. \tag{2.45a}$$

Let us first note that Eq. (2.45a) imply that both u and v separately satisfy the Laplace equation. Thus, we essentially could have applied the same homogeneous boundary condition that we have constructed for p, see Eq. (2.35), to velocities as well. However, we will rather construct the ABCs for velocities directly on the basis of the Cauchy–Riemann system. This will simplify the analysis for the zeroth Fourier mode, which was "problematic" in Section 2.2.1.

As before, we will construct the ABCs as vector relations on the model plane ζ and then use them with no changes on the physical plane z. On the model plane $\zeta = \xi + \mathrm{i}\eta$ the quantities u and $-v$ also satisfy the Cauchy–Riemann equations:

$$\frac{\partial u}{\partial \xi} = -\frac{\partial v}{\partial \eta}, \qquad \frac{\partial u}{\partial \eta} = \frac{\partial v}{\partial \xi}. \tag{2.45b}$$

The boundary conditions for velocities will actually be constructed on the basis of Eq. (2.45b).

Let us introduce polar components of the velocity vector $\boldsymbol{u}$

$$u_\rho = u\cos\theta + v\sin\theta, \qquad u_\theta = -u\sin\theta + v\cos\theta, \tag{2.46}$$

and rewrite the Cauchy–Riemann equations (2.45b) in polar coordinates

$$\frac{\partial(\rho u_\rho)}{\partial \rho} = -\frac{\partial u_\theta}{\partial \theta}, \qquad \frac{\partial(\rho u_\theta)}{\partial \rho} = \frac{\partial u_\rho}{\partial \theta}. \tag{2.47}$$

Denote $\boldsymbol{q} = [u_\rho, u_\theta]^t$ and represent Eq. (2.47) as a matrix equation

$$\frac{\partial(\rho \boldsymbol{q})}{\partial \rho} = \boldsymbol{A}\frac{\partial \boldsymbol{q}}{\partial \theta}, \tag{2.48}$$

where

$$\boldsymbol{A} = \begin{bmatrix} 0 & -1 \\ 1 & 0 \end{bmatrix}. \tag{2.49}$$

For the Fourier coefficients $\hat{\boldsymbol{q}}_k = \hat{\boldsymbol{q}}_k(\rho)$ we obtain from Eq. (2.48):

$$\frac{\mathrm{d}(\rho \hat{\boldsymbol{q}}_k)}{\mathrm{d}\rho} = \mathrm{i}k\boldsymbol{A}\hat{\boldsymbol{q}}_k, \quad k = 0, \pm 1, \pm 2, \ldots \tag{2.50}$$

We now diagonalize the matrix $\boldsymbol{A}$ of Eq. (2.49) and obtain:

$$\boldsymbol{A}\boldsymbol{K} = \boldsymbol{K}\boldsymbol{\Lambda}, \tag{2.51}$$

where

$$\boldsymbol{\Lambda} = \begin{bmatrix} \mathrm{i} & 0 \\ 0 & -\mathrm{i} \end{bmatrix}, \qquad \boldsymbol{K} = \begin{bmatrix} 1 & 1 \\ -\mathrm{i} & \mathrm{i} \end{bmatrix}. \tag{2.52}$$

Introducing $\hat{\boldsymbol{s}}_k = \boldsymbol{K}^{-1}\hat{\boldsymbol{q}}_k \Longleftrightarrow \hat{\boldsymbol{q}}_k = \boldsymbol{K}\hat{\boldsymbol{s}}_k$, we get instead of Eq. (2.50):

$$\frac{\mathrm{d}(\rho\hat{\boldsymbol{s}}_k)}{\mathrm{d}\rho} = \mathrm{i}k\boldsymbol{\Lambda}\hat{\boldsymbol{s}}_k, \quad k = 0, \pm 1, \pm 2, \ldots \tag{2.53}$$

Eq. (2.53) immediately yields

$$\hat{\boldsymbol{s}}_k = \begin{bmatrix} C_1^{(k)}\rho^{-k-1} \\ C_2^{(k)}\rho^{k-1} \end{bmatrix}, \tag{2.54}$$

where $C_1^{(k)}$ and $C_2^{(k)}$ are constants (different for different ks). Going back from representation (2.54) to the old variable $\hat{\boldsymbol{q}}_k$, we have (the matrix $\boldsymbol{K}$ is given by Eq. (2.52)):

$$\hat{\boldsymbol{q}}_k = \boldsymbol{K}\hat{\boldsymbol{s}}_k = \begin{bmatrix} C_1^{(k)}\rho^{-k-1} + C_2^{(k)}\rho^{k-1} \\ -\mathrm{i}C_1^{(k)}\rho^{-k-1} + \mathrm{i}C_2^{(k)}\rho^{k-1} \end{bmatrix} = \begin{bmatrix} \hat{u}_{\rho_k} \\ \hat{u}_{\theta_k} \end{bmatrix}. \tag{2.55}$$

Finally, introducing the inverse to the transformation (2.46)

$$u = u_\rho \cos\theta - u_\theta \sin\theta, \quad v = u_\rho \sin\theta + u_\theta \cos\theta, \tag{2.56}$$

and substituting the expressions

$$u = \sum_k \hat{u}_k \mathrm{e}^{\mathrm{i}k\theta}, \quad v = \sum_k \hat{v}_k \mathrm{e}^{\mathrm{i}k\theta}, \quad u_\rho = \sum_k \hat{u}_{\rho_k} \mathrm{e}^{\mathrm{i}k\theta}, \quad u_\theta = \sum_k \hat{u}_{\theta_k} \mathrm{e}^{\mathrm{i}k\theta},$$

into Eq. (2.56) we obtain

$$\sum_k \hat{u}_k \mathrm{e}^{\mathrm{i}k\theta} = \frac{1}{2}\sum_k \hat{u}_{\rho_k}\left(\mathrm{e}^{\mathrm{i}(k+1)\theta} + \mathrm{e}^{\mathrm{i}(k-1)\theta}\right) - \frac{1}{2\mathrm{i}}\sum_k \hat{u}_{\theta_k}\left(\mathrm{e}^{\mathrm{i}(k+1)\theta} - \mathrm{e}^{\mathrm{i}(k-1)\theta}\right),$$

$$\sum_k \hat{v}_k \mathrm{e}^{\mathrm{i}k\theta} = \frac{1}{2\mathrm{i}}\sum_k \hat{u}_{\rho_k}\left(\mathrm{e}^{\mathrm{i}(k+1)\theta} - \mathrm{e}^{\mathrm{i}(k-1)\theta}\right) + \frac{1}{2}\sum_k \hat{u}_{\theta_k}\left(\mathrm{e}^{\mathrm{i}(k+1)\theta} + \mathrm{e}^{\mathrm{i}(k-1)\theta}\right),$$

which implies

$$\hat{u}_k = \frac{1}{2}\hat{u}_{\rho_{k-1}} + \frac{\mathrm{i}}{2}\hat{u}_{\theta_{k-1}} + \frac{1}{2}\hat{u}_{\rho_{k+1}} - \frac{\mathrm{i}}{2}\hat{u}_{\theta_{k+1}}, \qquad \hat{v}_k = \frac{-\mathrm{i}}{2}\hat{u}_{\rho_{k-1}} + \frac{1}{2}\hat{u}_{\theta_{k-1}} + \frac{\mathrm{i}}{2}\hat{u}_{\rho_{k+1}} + \frac{1}{2}\hat{u}_{\theta_{k+1}}. \tag{2.57}$$

The last step is to substitute Eq. (2.55) into Eq. (2.57):

$$\hat{u}_k = C_1^{(k-1)}\rho^{-k} + C_2^{(k+1)}\rho^k, \qquad \hat{v}_k = -\mathrm{i}C_1^{(k-1)}\rho^{-k} + \mathrm{i}C_2^{(k+1)}\rho^k. \tag{2.58}$$

Representation (2.58) is valid for all ks including $k = 0$. Contrary to the general solution of the Laplace equation for $k = 0$: $C_1 + C_2 \ln\rho$, see Section 2.2.1, we do not have a growing logarithmic mode in representation (2.58) for $k = 0$. This constitutes a principal difference compared to the previously analyzed case and also gives the primary reason why we construct the ABCs for velocities directly from the Cauchy–Riemann system (2.45b) rather than first reduce it to two separate Laplace's equations for u and v.

The physical boundary conditions for velocities at infinity are obvious: the vector field $\boldsymbol{u}$ has to approach its free-stream value $\boldsymbol{u}_0$ as $|z| \to \infty$. As $\zeta(\infty) = \infty$, the value of $\boldsymbol{u}$ at infinity on the model plane ζ is also $\boldsymbol{u}_0$ and thus the boundary condition at infinity on the plane ζ is the same as on the plane z: $\boldsymbol{u} \to \boldsymbol{u}_0$ as $|\zeta| \to \infty$. This, in particular, implies boundedness of the vector field $\boldsymbol{u}$ at infinity. Then, from formula (2.58) we conclude that we need to require that $C_2^{(k+1)} = 0$ for $k > 0$ and

$C_1^{(k-1)} = 0$ for $k < 0$; for $k = 0$ both $C_1^{(-1)}$ and $C_2^{(1)}$ are allowed. Therefore, for $k \neq 0$ in the continuous framework we obtain analogously to Eq. (2.22a):

$$\begin{aligned} &\left.\frac{\mathrm{d}\hat{u}_k}{\mathrm{d}\rho}\right|_{\rho=R} + \left.\frac{|k|}{R}\hat{u}_k\right|_{\rho=R} = 0, \quad k = \pm 1, \pm 2, \ldots, \\ &\left.\frac{\mathrm{d}\hat{v}_k}{\mathrm{d}\rho}\right|_{\rho=R} + \left.\frac{|k|}{R}\hat{v}_k\right|_{\rho=R} = 0, \quad k = \pm 1, \pm 2, \ldots, \end{aligned} \tag{2.59}$$

and in the discrete framework, analogously to Eq. (2.34a):

$$\begin{aligned} &\hat{u}_{k,J+1}\left(\frac{|k|}{2} + \frac{\rho_{J+1/2}}{\Delta\rho_{J+1/2}}\right) = -\hat{u}_{k,J}\left(\frac{|k|}{2} - \frac{\rho_{J+1/2}}{\Delta\rho_{J+1/2}}\right), \quad k = -\frac{M}{2}+1, \ldots, -1, 1, \ldots, \frac{M}{2}, \\ &\hat{v}_{k,J+1}\left(\frac{|k|}{2} + \frac{\rho_{J+1/2}}{\Delta\rho_{J+1/2}}\right) = -\hat{v}_{k,J}\left(\frac{|k|}{2} - \frac{\rho_{J+1/2}}{\Delta\rho_{J+1/2}}\right), \quad k = -\frac{M}{2}+1, \ldots, -1, 1, \ldots, \frac{M}{2}. \end{aligned} \tag{2.60}$$

The only difference between Eqs. (2.60) and (2.34a) is that in Eq. (2.60) we have $|k|$ instead of $|\alpha_k|$. As has been shown, α_k in Eq. (2.34a) comes from the central-difference second-order discretization of the Laplacian (2.28) that we do not use for velocities. It is obvious, however, that for small $\Delta\theta$ and small k (long waves), we have $\alpha_k^2 \approx k^2$ (see Eq. (2.31)).

For $k = 0$, the difference between the boundary conditions for velocities and the corresponding boundary conditions for the pressure is significant. As we do not have to worry about canceling the growing logarithmic modes for velocities, and as we know the free-stream value of the velocity vector $\boldsymbol{u}_0 = [U, V]^t$, we simply have

$$\hat{u}_{0,J+1} = U, \quad \hat{v}_{0,J+1} = V. \tag{2.61}$$

The meaning of boundary conditions (2.61) is transparent – the correct value of the solution at infinity, i.e., the correct constant, is picked up on the zeroth Fourier mode, all other Fourier modes in the solution vanish at infinity.

Formulae (2.60) and (2.61) constitute the global ABCs for velocities. It is interesting to note that as the momentum equations are actually integrated by means of downstream marching, the information provided by boundary conditions (2.60) and (2.61) is used only on the inflow portion of the artificial boundary. As, however, the computations show, the values of $\boldsymbol{u}$ on the outflow portion of the boundary obtained with the global boundary conditions very well agree with the actual values obtained by the downstream integration through the domain, see Section 3.4.

2.3. Combined formulation and implementation

The values of the solution at the ghost points, i.e., on the $(J+1)$th gridline, are obtained by applying the ABCs of Sections 2.2.1 and 2.2.2 to the current approximation on the outer boundary, i.e., on the Jth gridline. This is followed by a relaxation sweep. The aforementioned two steps form the combined relaxation sweep.

We note that implementation of global ABCs (2.44) for the pressure, as well as similar boundary conditions for velocities (see Eq. (2.60)), is numerically inexpensive. Indeed, formula

(2.35) suggests that each application of these boundary conditions requires two discrete Fourier transforms along the outer boundary, which costs $\mathcal{O}(M \log M)$ arithmetic operations provided the FFT is employed. There are also additional arithmetic operations (multiplication by β_k, see Eq. (2.35), and averaging $\bar{f}_{\cdot,J}$, see Eq. (2.44)) with the total count proportional to M. Altogether, the cost of implementation of global ABCs is linear times logarithm with respect to only circumferential grid dimension, whereas the cost of the relaxation sweep is obviously proportional to the overall grid dimension $M \cdot J$. As such, computational overhead associated with global ABCs is essentially negligible.

We apply a standard multigrid algorithm known as the full approximation scheme (FAS). The only "nonstandard" aspect that requires special attention is the application of the ABCs for the pressure on the coarser grids, because these ABCs involve the conservation issue outlined in Section 2.2.1.

The pressure equation on the finest grid can be written as follows

$$L^h p^h = f^h,$$

where L^h is the discrete Laplacian and f^h is the forcing term as defined earlier. The fine grid equation residual is given by

$$r^h = f^h - L^h p^h.$$

Then, the FAS coarse grid equation is

$$L^H p^H = f^H,$$

where

$$f^H = L^H I_h^H p^h + \hat{I}_h^H r^h,$$

and I_h^H and $\hat{I}_h^H$ are the restriction operators. The operator I_h^H is a standard injection operator, and the operator $\hat{I}_h^H$ is also a standard full-weighting operator.

Let us note that since $\hat{I}_h^H$ is a "conservative" operator, the coarse-grid right-hand side f^H possesses the same telescopic property as the fine-grid right-hand side f^h has. This means that it is composed of flux contributions through the control volume boundary, and for a pair of neighboring control volumes the contributions from fluxes through the common interface cancel one another. Therefore, by summing up the source terms f^H on the coarse grid we again arrive at the total flux through the outer faces of the control volumes centered at the nodes of the Jth gridline, i.e., the quantity $\sum_{m=0}^{M-1} G^f_{m,J+1/2}$, see formula (2.43), (the index J refers here to the coarse grid) in the same way as we have done that on the fine grid.

As the pressure in an incompressible flow problem is defined only up to an additive constant, the uniqueness of the solution is achieved by keeping its value fixed and equal to an initially prescribed quantity at one of the nodes on the coarsest grid throughout the entire computation.

We should also mention that another way of implementing the non-local ABCs, which has not been actually tried yet, consists of using relation (2.44) to actually eliminate the ghost cells and thus solve iteratively only for the variables on the original grid. The properties of the ABCs' matrix $\boldsymbol{T}$ obtained in Section 2.2.1, see the discussion right after formula (2.37), may then help to establish and analyze the properties of the overall system matrix from the standpoint of convergence and convergence rate of the (multigrid) iterations.

3. Numerical experiments

3.1. Test problems

One test problem considered here is the incompressible, irrotational flow around a symmetric airfoil. A circular cylinder is transformed into an airfoil by the Kármán–Trefftz transformation,

$$\frac{z+2}{z-2} = \left(\frac{\zeta+1}{\zeta-2}\right)^{2-\epsilon/\pi} \tag{3.1}$$

where ζ is the complex coordinate in the circle plane, z is the complex coordinate in the physical plane, and ϵ is the trailing-edge angle. The cylinder in the ζ-plane is centered at $\zeta = (-0.1, 0)$ with a radius of 1.1. The trailing edge angle ϵ is 10°. This generates an airfoil with a thickness ratio of approximately 15% in the z-plane.

The grids are generated by using a uniform azimuthal spacing around the cylinder in the ζ-plane. The spacing in the radial direction is stretched such that the cell aspect ratio is equal to one everywhere. The dimensions of the grids that we have used are given in the next section, see Table 1.

Besides the airfoil flow, and primarily for the reasons of comparing the numerical performance for different geometries, we have also calculated an irrotational flow around a circular cylinder. This is the same cylinder as the one we substituted into the transformation (3.1) to obtain the Kármán–Trefftz airfoil. Thus, for the cylinder case the planes z and ζ coincide and the flow around the cylinder is calculated on the actual polar grid.

Only non-lifting solutions are considered hereafter for both the airfoil and cylinder, so the freestream flow is aligned with the x-direction.

3.2. Computational setting

The actual dimensions and approximate geometric sizes of the grids that we have used for our calculations are presented in Table 1.

Approximate locations of the boundary in Table 1 are given with respect to the center of the cylinder (i.e., circle) or airfoil; in the latter case the location closest to the airfoil surface is presented.

On each grid shown in Table 1 we have calculated a non-lifting incompressible inviscid flow with a given free-stream speed. The discrete flow solution is calculated by applying multigrid iterations to the elliptic part of the factorized system (pressure) and using a downstream marching

Table 1
Grid dimensions and sizes

Grid dimension: angular × radial	129 × 129	129 × 65	129 × 33	129 × 17	129 × 9
Approximate location of the outer boundary for the cylinder case measured in diameters	272.5	11.5	2.5	1.1	0.75
Approximate location of the outer boundary for the airfoil case measured in chords	135	6	1.25	0.55	0.37

algorithm for the advection part (velocities), see Section 2.3. We employ a FAS multigrid W(2,1) cycle, with full weighting restriction and full coarsening [10]. The number of nested grids for each computation is determined by the dimension of the finest grid (see Table 1), i.e., the number of possible subdivisions by two. On the coarsest grid we find the "exact" solution by performing sufficiently many relaxation sweeps. For a pure Laplace or Poisson equation on the grids of the kind presented in Table 1, the smoothing rate for a lexicographic Gauss–Seidel relaxation is 0.5 per one sweep [10]. Therefore, for a W(2,1) cycle the "predicted" or ideal convergence rate is $0.5^{(2+1)} = 0.125$ per cycle, i.e., the residual should drop by a factor of $1/8$ in a single multigrid cycle.

Actually, we have calculated two types of flow solutions. First, we were solving for the pressure only while keeping the velocity field frozen on the grid with the values taken from the exact solution. Next, we solved the full Euler system as well. The ideal convergence rate of about 0.125 per cycle was indeed observed in our computations when we were solving for the pressure only, see Section 3.3. As concerns the true Euler solution, if we were to fully separate the elliptic and hyperbolic factors in the Euler equations, we should have seen the exact same convergence rate. In fact, we observed a somewhat slower convergence when solving the full Euler equations, see Section 3.4. The reason for the discrepancy is not related to the treatment of the external artificial boundary as the slowdown takes place for all three types of the ABCs that we employ, see below. Convergence deterioration that we observe is rather caused by the following. It has been mentioned in Section 2.1 that the subprincipal terms in this equation can be disregarded when constructing the relaxation scheme. However, near the stagnation point this may be not legitimate. A possible implication of this, i.e., loss of efficiency, is discussed in the recent paper [16].

For each variant of the computation (determined by the geometry and the grid, see Table 1), we have used three types of external ABCs. The first boundary conditions are of the Dirichlet type for all three flow quantities, the actual data to specify at the outer boundary are taken from the available exact solution. This is apparently the best possible treatment for the artificial boundary and henceforth these ABCs will be referred to as exact. The second boundary conditions are global ABCs described in Section 2.2, hereafter they will be referred to as global. Finally, the third boundary conditions are local; they are set as follows. In the course of the relaxation procedure, the residuals of the pressure equation are evaluated near the outer boundary on "halves-cells" using the condition $\frac{\partial p}{\partial \boldsymbol{n}}\big|_{\text{outer}} = 0$, where $\boldsymbol{n}$ is the normal direction to the boundary. Besides, at each point on the outer boundary we specify the flow angle, which is approximately taken to be equal to that at infinity (i.e., to the angle of attack). Finally, to calculate the magnitude of the velocity, we use the conservation of the total pressure and the corresponding value of the static pressure that has just been updated. The local approach is obviously the simplest of the three in the sense that local ABCs are easier to construct and implement than the global ones and at the same time they can be used when the exact solution is not available.

The purpose of conducting the foregoing series of computations on different grids (see Table 1) with different ABCs is to compare the multigrid convergence rates as they depend on the type of ABCs and domain size. We will also be comparing the accuracy of the numerical solutions as it depends on the domain size and the type of the ABCs. These two characteristics – convergence rate (i.e., numerical efficacy) and accuracy – are obviously of the foremost importance when designing any numerical algorithm.

Since the solutions that we have calculated develop neither lift nor drag, the accuracy is assessed not by examining integral characteristics of the flow, like lift and drag coefficients (as typical for many CFD studies), but rather by comparing the actual error profiles for different flow quantities.

3.3. Solving for the pressure only

In this section we describe and analyze the numerical results for two cases – non-lifting flow past a circular cylinder and non-lifting flow past an airfoil. As has been mentioned, the velocity field on the grid for this series of computations is considered known, we actually take it from the exact solution obtained using classical complex variable technique.

3.3.1. Circular cylinder

In Fig. 3 we present the results obtained with the exact far-field ABCs, both convergence history and surface pressure error, for the flow past a circular cylinder. In Figs. 4 and 5 we present similar results obtained with the global and local far-field ABCs, respectively.

From Figs. 3(A) and 4(A) one can easily conclude that for the exact and global ABCs we have been able to obtain the multigrid convergence rate according to the theoretical prediction – roughly one order of magnitude reduction of the pressure residual per one W(2,1) multigrid cycle. As concerns local ABCs, from Fig. 5(A) we see that the same is true only for the sufficiently large grids, 129×129 and 129×65, and consequently, large domains, see Table 1, whereas for smaller domains the convergence slows down.

To assess the accuracy we compare the profiles of the relative error in pressure (we can calculate it explicitly as the exact solution is known) on the surface of the cylinder. Figs. 3(B) and 4(B) show that for the exact and global ABCs this relative error is always below the 10^{-2} level, i.e., 1%,

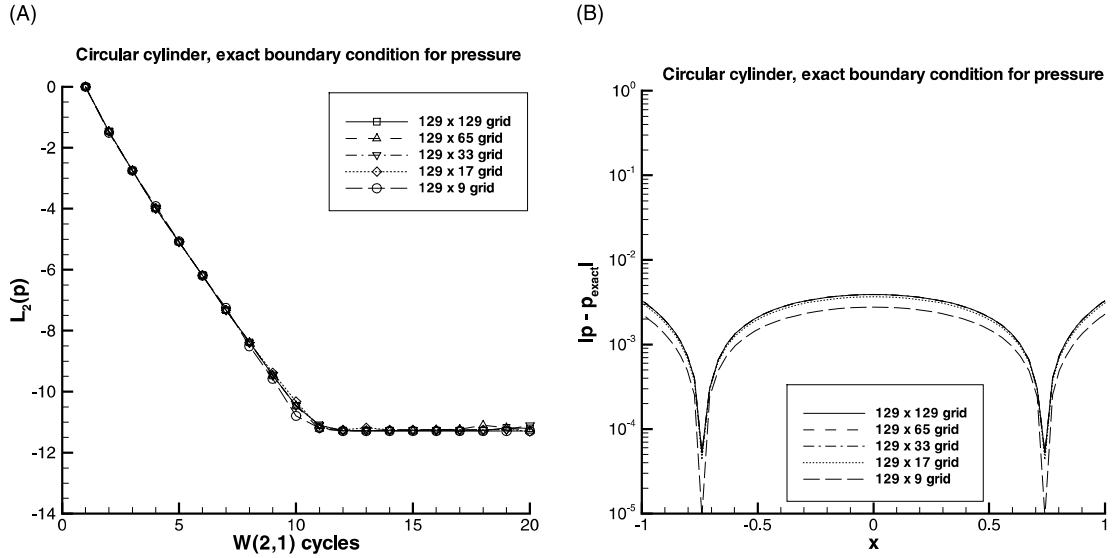

Fig. 3. Computation of the flow past a circular cylinder using exact ABCs. (A) Convergence history and (B) surface error.

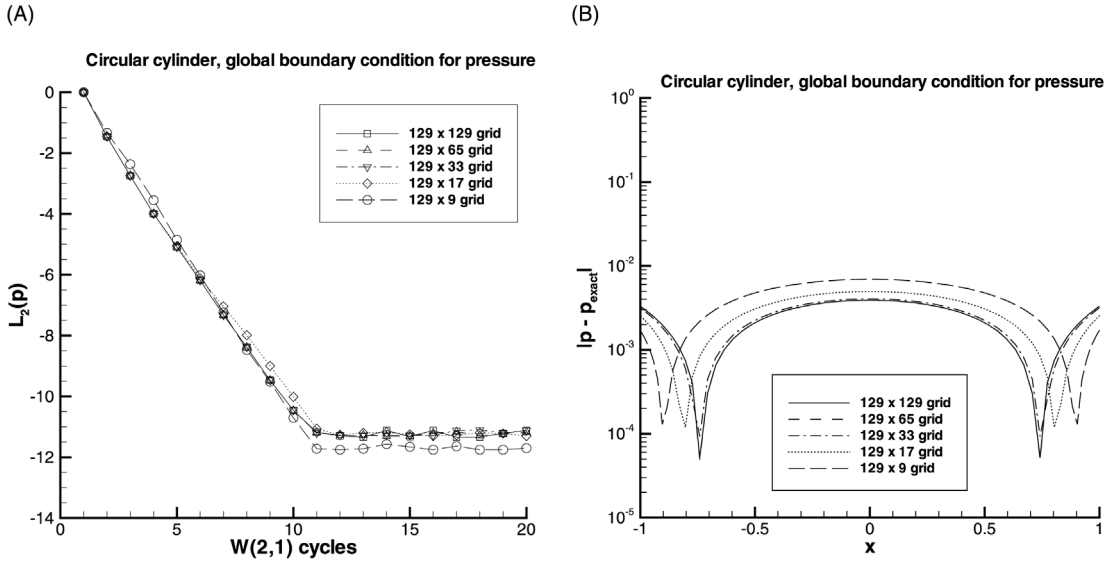

Fig. 4. Computation of the flow past a circular cylinder using global ABCs. (A) Convergence history and (B) surface error.

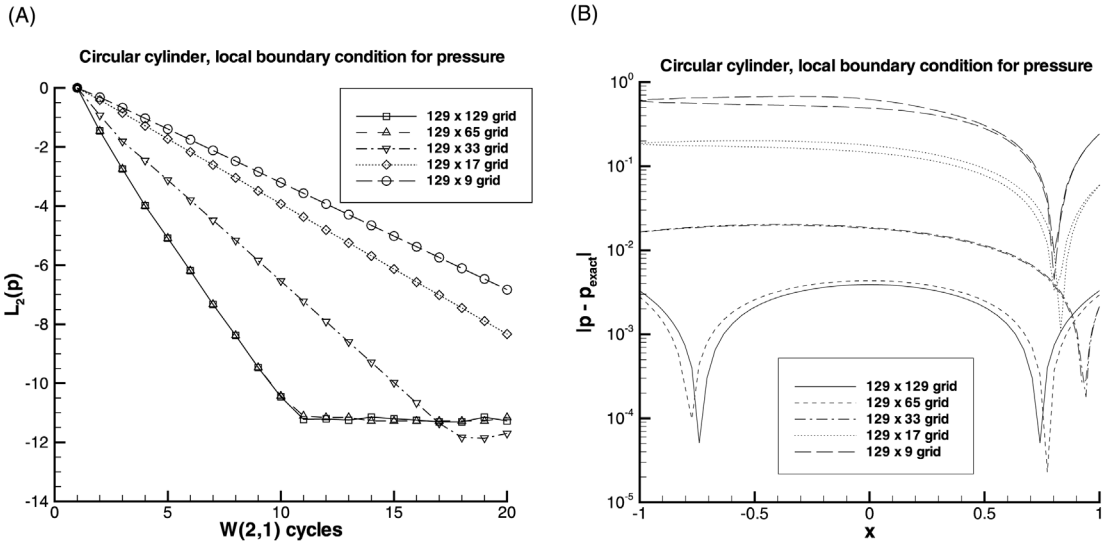

Fig. 5. Computation of the flow past a circular cylinder using local ABCs. (A) Convergence history and (B) surface error.

for all grids. For the local ABCs the accuracy level better than 1% can be obtained again only for the two largest grid dimensions, 129×129 and 129×65. With the reduction of the grid dimension and, accordingly, domain size (see Table 1), the accuracy deteriorates and eventually reaches the value $\mathcal{O}(1)$ for the smallest grid 129×9, see Fig. 5(B). Besides, Fig. 5(B) shows that for the smaller

domains (129×17 and 129×9) the flow develops some spurious non-physical asymmetries. Indeed, the two close lines of the same dash pattern on Fig. 5(B) correspond to the error profiles on the upper and lower surfaces of the cylinder for a particular grid. Theoretically, these two lines should be indistinguishable, which is the case for the larger domains; the actual discrepancy that we observe for the smaller domains indicates the presence of asymmetry.

Summarizing for this case, we see that the exact and global ABCs perform equally well for domains of all sizes, whereas the performance of the local ABCs noticeably degrade with the shrinkage of the domain.

3.3.2. Kármán–Trefftz airfoil

In Fig. 6 we present computational results obtained with the exact far-field ABCs, both convergence history and surface pressure error, for the non-lifting flow past a Kármán–Trefftz airfoil with the 10° trailing edge angle. In Figs. 7 and 8 we present similar results obtained with the global and local far-field ABCs, respectively.

As concerns multigrid convergence rate in this case, from Figs. 6(A) and 8(A) we see that for the exact and local ABCs, respectively, we have been able to recover it according to the theoretical prediction (Section 3.2). The multigrid convergence rate for global ABCs, see Fig. 7(A), is also obtained according to the theoretical prediction – about one order of magnitude reduction of the residual level per one W(2,1) multigrid cycle, but for smaller grids the residual never reaches the machine zero. Instead, starting from some level specific for each grid, the convergence curve "flattens" and the residual does not drop any further, see Fig. 7(A). We postpone the discussion of why, in our opinion, this phenomenon occurs till Section 3.3.3. Now we only emphasize that the level at which the residual flattens, see Fig. 7(A), is well below (several orders of magnitude) the

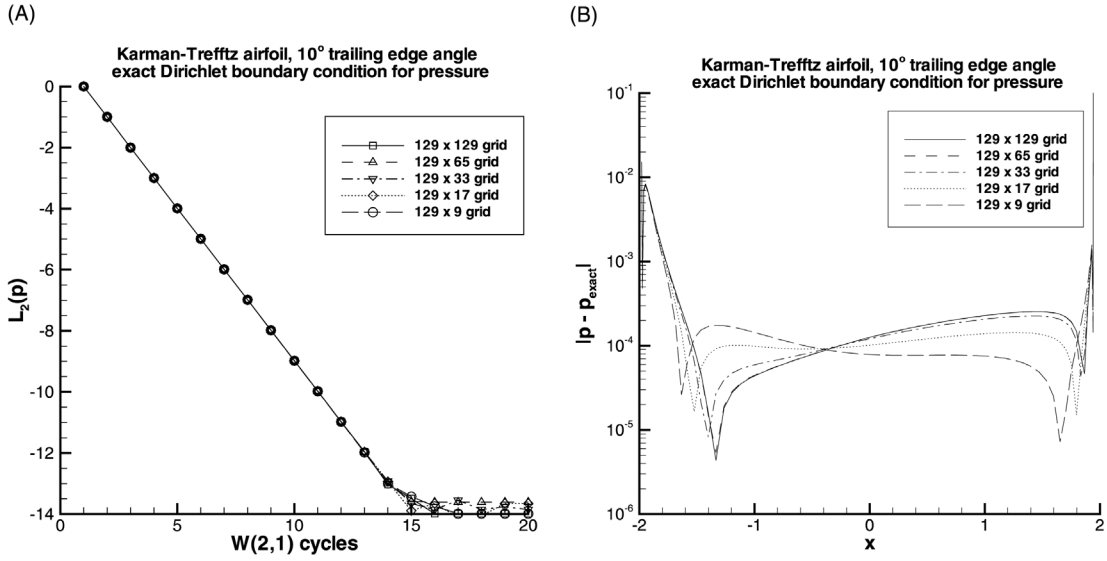

Fig. 6. Computation of the flow past an airfoil using exact ABCs. (A) Convergence history and (B) surface error.

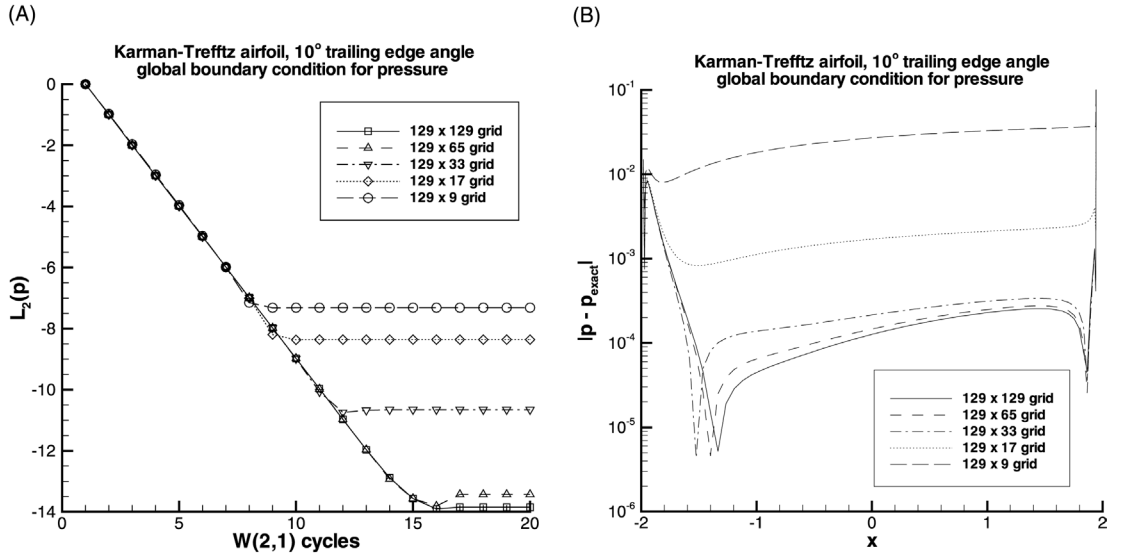

Fig. 7. Computation of the flow past an airfoil using global ABCs. (A) Convergence history and (B) surface error.

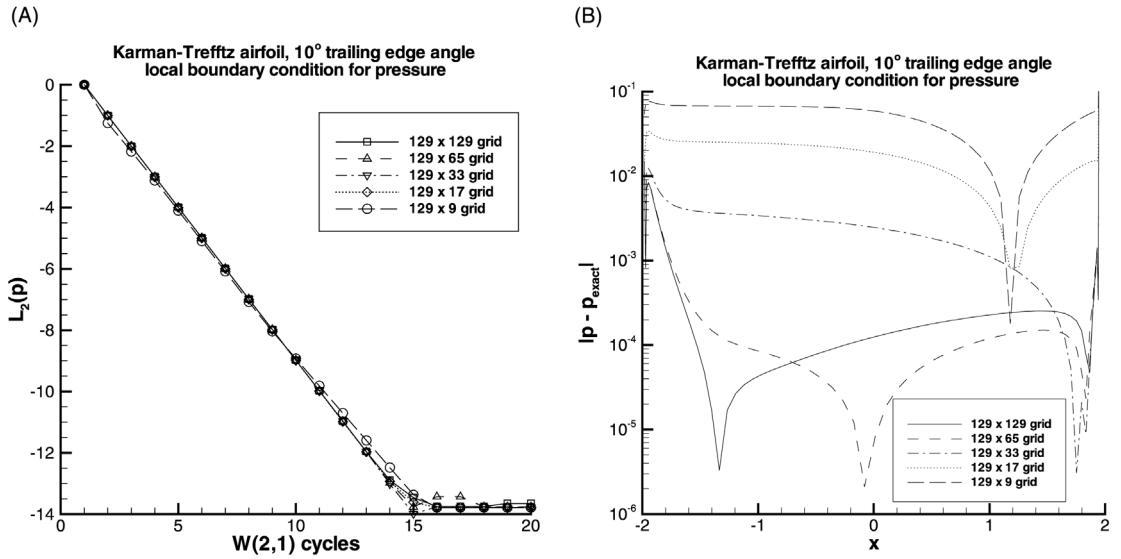

Fig. 8. Computation of the flow past an airfoil using local ABCs. (A) Convergence history and (B) surface error.

truncation error level for all the cases that we have studied. Therefore, we do not expect that this phenomenon will affect the final accuracy of the solution in any respect.

Indeed, for the exact boundary conditions the accuracy for all grids is about $\sim 10^{-4}$, see Fig. 6(B), except in the small areas near the leading and trailing edges. In these areas we are, in fact, encountering the well recognized problems with the approximation. Indeed, at the trailing edge,

the conformal mapping that we use for generating the grid has a singularity, therefore the surface normal is not well defined there. Instead of accounting for this singularity analytically when developing the discretization we effectively "ignore" it and apply the nontranspiration boundary condition by evaluating the surface normal at the trailing edge in the same way as we do over the rest of the airfoil surface, by finite differences of the surface coordinates. At the leading edge, the numerical viscosity apparently dominates the behavior locally, so there is an artificial dissipative error that corrupts the total pressure. However, the latter problems have no direct relation to the treatment of the outer boundary, which is the subject of the current study.

Comparing the accuracy provided by the exact ABCs to the one that we obtain with the global ABCs, i.e., comparing Figs. 6(B) and 7(B), we see that for the first three grids, 129×129, 129×65, and 129×33, global ABCs provide for the same accuracy as the exact ones do, i.e., about 10^{-4}. For the next smaller grid, 129×17, the accuracy with the global ABCs is $\sim 10^{-3}$, and for the smallest grid 129×9 this accuracy is $\sim 10^{-2}$. Thus, it turns out that in terms of accuracy global ABCs perform somewhat worse than the exact ones on small computational domains (see Table 1) for this airfoil case. It is clear, however, that the accuracy that we do recover with the global ABCs, see Fig. 7(B), is still acceptable for all purposes. We also note that the exact ABCs are obviously not available in realistic situations, while global ABCs can be constructed, e.g., on the basis of the DPM, see Ref. [21].

One might think that the slowdown of convergence that we observe for global ABCs on the smaller grids, see Fig. 7(A), and the slight deterioration of accuracy that we also observe for these boundary conditions on the smaller grids, see Fig. 7(B), could be related to one another. We claim that this is, in fact, not so, because for the local ABCs that do provide in this case for the optimal convergence till the machine zero on all grids, see Fig. 8(A), the accuracy rapidly deteriorates as the domain shrinks, see Fig. 8(B), and reaches the level $\sim 10^{-1}$, i.e., 10%, for the smallest grid 129×9.

Summarizing for the airfoil case, we see that the global ABCs actually perform only slightly worse than the exact ones and their accuracy is certainly within the practically acceptable limits on all grids, whereas the solutions obtained with the local ABCs rapidly lose accuracy as the domain size reduces.

3.3.3. Comparison of the cylinder and airfoil computations

The first easy observation that one can make is that on the average the relative accuracy for the Kármán–Trefftz airfoil is better than that for the circular cylinder for all the computations that we have conducted, see Figs. 3(B)–8(B). With no rigorous explanation we can attribute this to the mere fact that in some sense a "thick" cylinder introduces more of a perturbation into the flow that a "thin" airfoil does (the thickness ratio of the airfoil is 15%, see Section 3.1). The same fact apparently accounts for the slowdown of multigrid convergence on smaller domains when computing the flow past a cylinder with local ABCs, see Fig. 5(A), whereas the same local ABCs for the airfoil still provide for the optimal multigrid convergence rate, see Fig. 8(A). We emphasize here that the convergence slowdown on Fig. 5(A) (local ABCs for the cylinder) is different in nature to the one on Fig. 7(A) (global ABCs for the airfoil) because in the latter case we do recover the optimal convergence rate and lose it only toward the end of the computation, when the residuals are already sufficiently small, and in the former case the convergence is suboptimal from the very beginning.

The phenomenon of "flattening" of the residuals for global ABCs, see Fig. 7(A), can apparently be attributed to the following. The boundary conditions have actually been constructed on the conformal plane ζ, where the body is always a cylinder and the grid is always exactly polar, which, in particular, means orthogonal. In Sections 2.1 and 2.2.1 we have addressed the importance of maintaining the exact conservation on the grid from the standpoint of solvability and also shown (see Eqs. (2.40) and (2.43)) how to maintain the exact conservation on this particular grid, i.e., grid of polar coordinates. For the flow around the airfoil the discretization is built directly using finite volumes on the actual grid in the physical plane. For small domains, this grid may have slight numerical deviations from orthogonality even near the outer boundary. This, in turn, results in a slightly different discrete operator. (As has been mentioned in Section 2.2.1, in contrast to Eq. (2.28) it may contain diagonal nodes with small coefficients.) This may give rise to a minor violation of the overall conservation on the grid, the smaller the domain, the larger the violation. (Indeed, the left-hand side of Eqs. (2.40) and (2.43) has to have this particular form to be incorporated into the boundary conditions, and the conservation will now be achieved with a different operator.) This small "incompatibility" is responsible for the flattening of the convergence history curve (i.e., residual level vs. number of multigrid cycles, see Fig. 7(A)). A similar phenomenon was observed in Ref. [13] when solving a Neumann problem, for which the solvability condition was satisfied exactly for the continuous formulation, while only up to the truncation error level for the discrete formulation.

3.4. Solving the Euler system

Let us first note that in the framework of the full Euler system we are computing only the flow around the airfoil. The cylinder case analyzed in Section 3.3 can, in fact, be used only for the pure pressure computations. It is not suitable for the full Euler equations because the artificial dissipation of the scheme will result in flow separation. This effect is, again, due to the "thickness" of the cylinder.

In Fig. 9 we present convergence histories on all grids for all three types of the ABCs. As one can see, the convergence in all cases is somewhat slower than the theoretically predicted rate of 0.125 per one W(2,1) cycle that we use. The slowdown of the multigrid convergence that we observe here is obviously not related to the treatment of the artificial external boundary because it takes place for all three types of the ABCs. As mentioned in Section 3.2, this slowdown is most likely related to the apparently invalid omission of subprincipal terms near the stagnation point in the construction of the relaxation scheme. This issue is discussed in Ref. [16]. We also emphasize that for the local ABCs, see Fig. 9(C), the convergence is noticeably slower than for the other two types, see Figs. 9(A) and (B), and for the smallest grid 129×9 the solution with local ABCs does not converge at all. That is why we have only four curves (as opposed to five) plotted on Fig. 9(C).

In Figs. 10 and 11, we are showing the surface pressure error profiles for all five grids and three types of the ABCs that we have used. As has been mentioned, the solution with local ABCs on the smallest grid 129×9 did not converge, therefore the corresponding error curve is not available. (Note, as opposed to Section 3.3, here we present separate error profile plots for each grid and all three types of the ABCs, i.e., have three curves per plot, rather than showing five curves from all five grids on one plot for each geometry and each type of ABCs.)

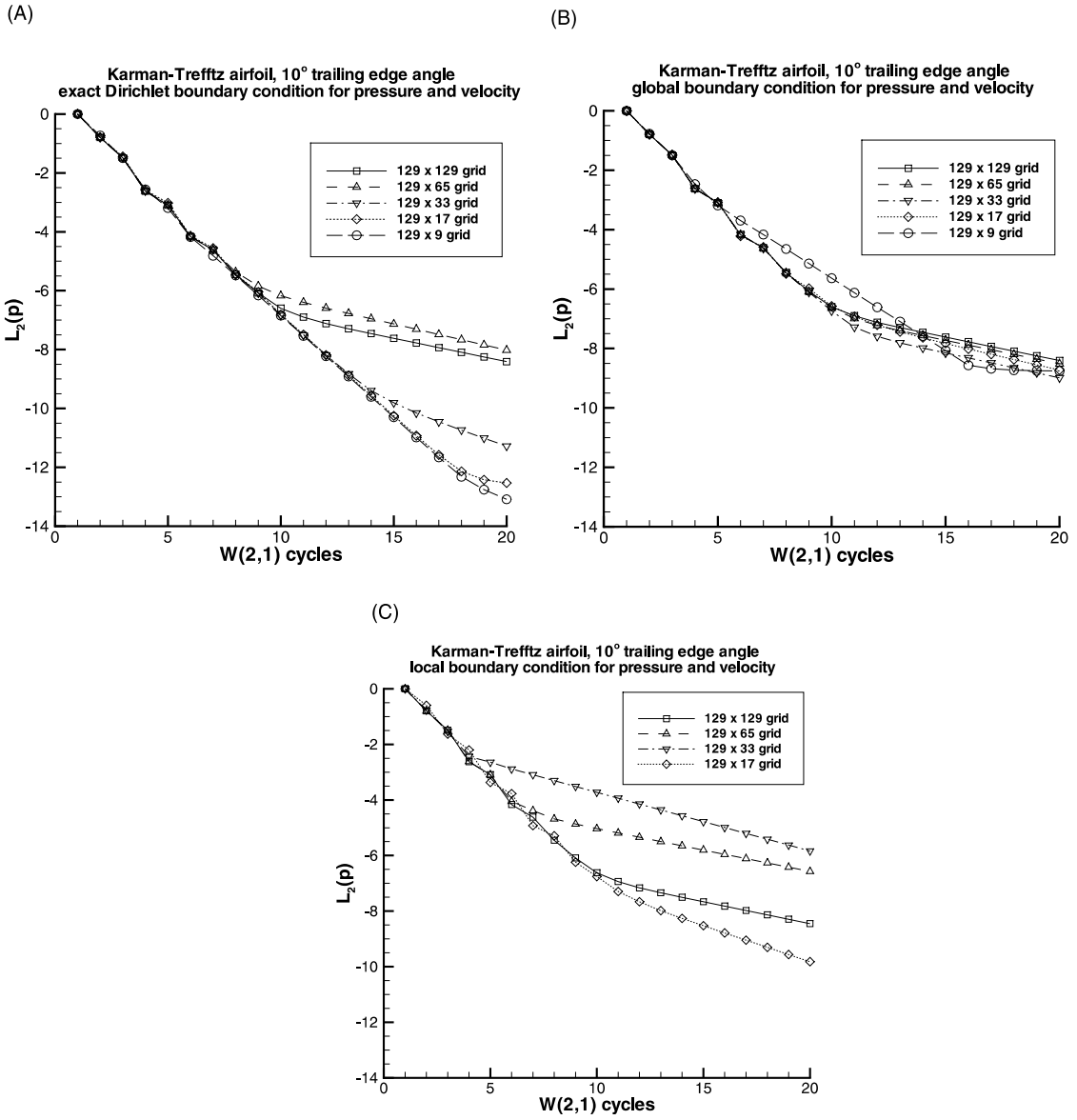

Fig. 9. Convergence histories for the flow past an airfoil computed in the framework of the full Euler equations. (A) Exact ABCs, (B) global ABCs and (C) local ABCs.

Figs. 10 and 11 allow one to conclude that for the exact ABCs the surface pressure error is always below the 10^{-2} level, for global ABCs it is also below than 10^{-2}, except for the smallest domain, for which it is only slightly above the level of 10^{-2}, i.e., 1%. For local ABCs the accuracy rapidly deteriorates with the domain size decrease and eventually reaches $\mathcal{O}(1)$ on the grid of moderate dimension 129×17 before the solution breaks on the smallest grid 129×9.

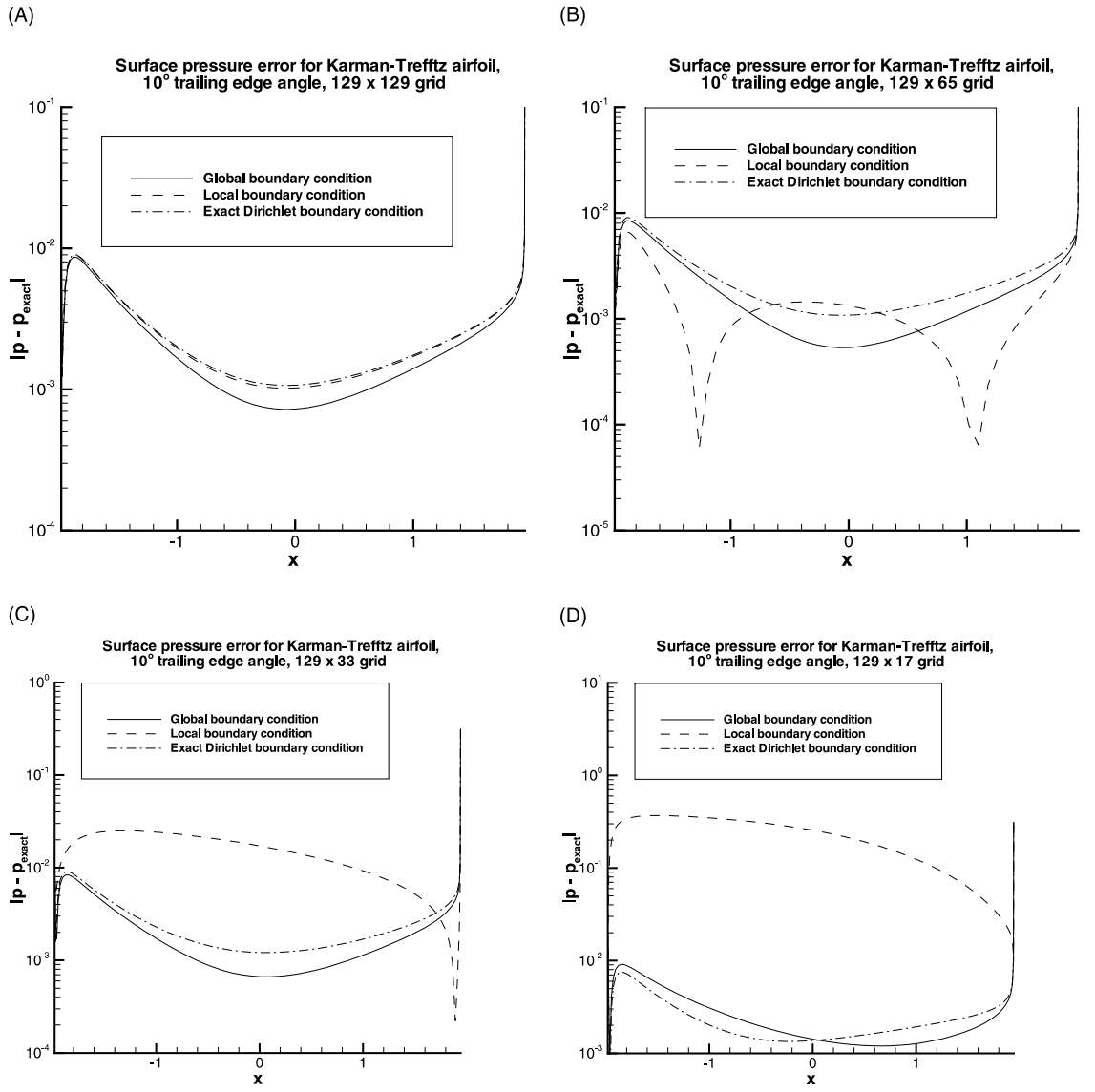

Fig. 10. Surface pressure error profiles for the flow past an airfoil computed in the framework of the full Euler equations.

As opposed to Section 3.3, here we are computing all three flow quantities rather than only pressure. Therefore, we also compare error profiles for velocities. In Fig. 12 we present velocity errors for the smallest grid, on which all three solutions converged, i.e., for the grid 129×17. Fig. 12(A) shows that both the exact and global ABCs perform equally well for the surface velocity (the error is slightly above 10^{-2}) and the solution obtained with local ABCs substantially lacks

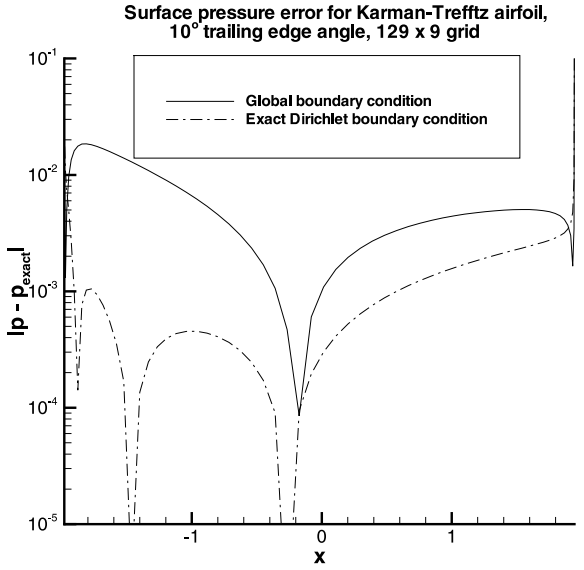

Fig. 11. Surface pressure error profiles for the flow past an airfoil computed in the framework of the full Euler equations.

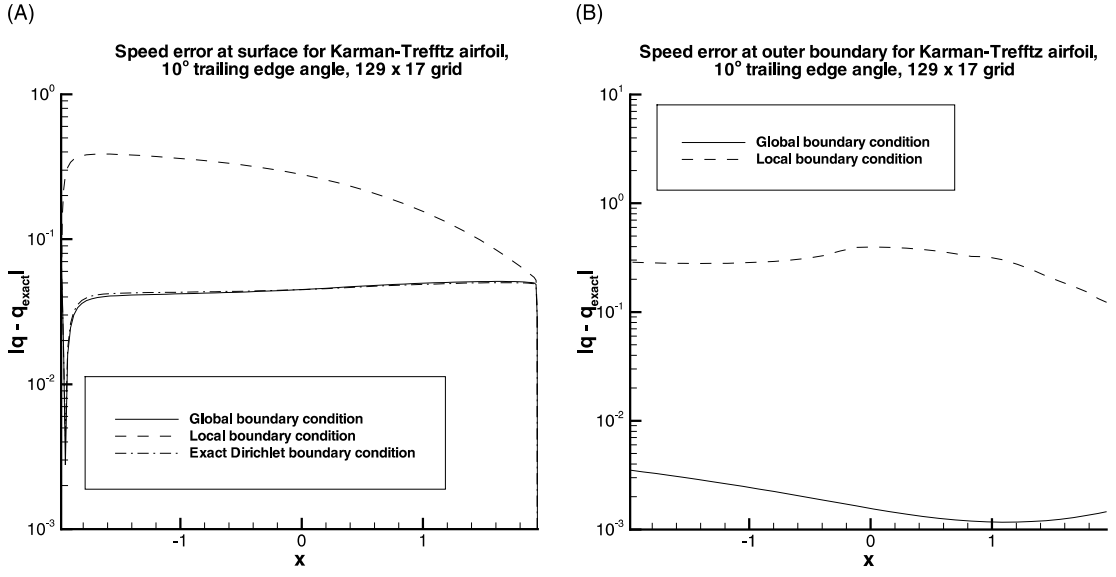

Fig. 12. Velocity error profiles for the flow past an airfoil computed in the framework of the full Euler equations on the 129×17 grid. (A) On the surface and (B) on the outer boundary.

accuracy. At the outer boundary, see Fig. 12(B), global ABCs provide for the error level below 10^{-2}, whereas local ABCs are lagging behind by roughly two orders of magnitude.

Note, we do not present the error curve for the exact ABCs on Fig. 12(B) because the Dirichlet data for these boundary conditions are taken from the exact solution and thus the corresponding error would have been identically equal to zero.

Summarizing for the full Euler airfoil case, we see that global ABCs are almost as good as the exact ones in terms of both the solution accuracy and multigrid convergence rate. As concerns global vs. local ABCs, from Figs. 9–12 we conclude that global ABCs clearly outperform the local ones from the standpoints of accuracy, convergence rate, and robustness. Accuracywise, they allow to reduce the grid dimension by a factor of 8–16 with no or very little increase in error and with the obvious corresponding reduction in computational costs – this is the primary result that we have expected. Regarding the robustness, global ABCs provided for the convergence on the smallest grid 129×9, when the algorithm with local ABCs simply failed to converge.

4. Discussion and conclusions

Motivated by the two independent successful developments in CFD that have appeared recently: The new factorizable schemes for the equations of hydrodynamics that facilitate the construction of optimally convergent multigrid algorithms, and highly accurate global far-field ABCs, we have built and tested a unified methodology for calculating incompressible flow solutions based on the combination of the two aforementioned approaches. The primary result that we have obtained is the following. Global ABCs do not hamper the optimal (i.e., unimprovable) multigrid convergence rate pertinent to the solver. At the same time, contrary to the standard local ABCs, the solution accuracy provided by the global ABCs deteriorates very slightly or does not deteriorate at all when the computational domain shrinks, which clearly translates into substantial savings of computer resources.

The combined methodology was developed for the most simple formulation of both the factorizable scheme and the ABCs: the so-called pressure-Poisson scheme, and the ABCs built semi-analytically using the separation of variables along the artificial boundary. The methodology was tested on a class of incompressible inviscid non-lifting two-dimensional flows with the exact solutions readily available through the implementation of the classical complex variable technique. On one hand, this intentionally elementary formulation (both theoretically and experimentally) allows to use the analytical approaches and results as much as possible for both constructing the methodology and numerically assessing its performance. On the other hand, this formulation still keeps the key fundamental principles, on which both the factorizable scheme and global ABCs are based, and thus should be regarded not as an isolated model example but rather as a foundation of the future approaches to more complex problems.

In a series of numerical tests (Section 3) we have compared three types of the ABCs: Exact Dirichlet ABCs obtained from the exact analytical solution, global ABCs, and standard local ABCs of the kind that is used extensively and routinely nowadays when neither the exact data nor any advanced methodology is available. From our computations we can conclude that convergencewise, global ABCs perform practically as good as the exact ones; in other words they recover the optimal multigrid convergence rate that cannot be improved. From the standpoint of accuracy, they allow for a very substantial reduction of the computational domain size, two orders of magnitude in terms of the actual diameter and at least one order of magnitude in terms of the grid

dimension, with no or very little deterioration in the final quality of the calculated solution. This obviously yields a considerable reduction in the corresponding computational costs, which altogether constitutes the primary result that we have expected.

The aforementioned reduction in the computational domain size is obtained when comparing the performance of the global ABCs with that of the standard local boundary conditions. We should emphasize here that as the exact ABCs are not attainable routinely, the comparative assessment of global and local methodologies is of the foremost importance from the viewpoint of computational practice. Our numerical experiments show that besides the solution accuracy, global ABCs clearly surpass the local ones from the standpoints of multigrid convergence rate and robustness. (The latter point refers to the case when global ABCs could provide for convergence while the local ones diverged.) A similar kind of behavior has been observed previously for the global DPM-based ABCs combined with the older suboptimal multigrid methodologies [21,25–27,30–33]. As at the moment different flavors of local boundary conditions still dominate the area of production computations in CFD, the new combined technique developed and tested in this paper provides a potential for creating new flow solvers far superior to those currently in use.

An important implementation lesson learned when building the unified methodology is that the inhomogeneities in the elliptic factor of the system have to be handled very carefully. In particular, the exact conservation on the grid has to be strictly enforced to guarantee the solvability of the discrete problem. Let us note that the actual inhomogeneity of the PPE that we have studied in this paper is not going to be encountered in the future because the forthcoming factorizable scheme for the incompressible case will be based on the Laplace equation for the velocity potential as an elliptic factor (always homogeneous). On the other hand, the current study provides foundation for treating the compressible flow equations, in which the full-potential part will always involve far-field inhomogeneities due to the sub-principal terms. The boundary conditions for this equation will be the same as those we have studied here: Neumann's boundary condition on the solid wall and requirement of boundedness of the solution at infinity. Therefore, the conclusions of the current study, in particular those related to the solvability issues, are going to be useful.

Our future plans involve extensions along both experimental and theoretical lines. Numerically, we will incorporate a different formulation of the scheme and study more complex cases, including compressible flows. Theoretically, we will try and analyze the properties of the discrete ABCs' operator (a generalization of the operator $\boldsymbol{T}$, see Eqs. (2.35) and (2.37)) in terms of the influence it may exert on multigrid convergence, e.g., whether the matrix of the corresponding overall system that is solved by iterations may appear either symmetric positive definite or an M-matrix (see Ref. [41] for the definition of the latter). Global ABCs for the more complex cases that we plan on studying in the future will be obtained using DPM.

References

[1] Murman EM, Cole JD. Calculation of plane steady transonic flows. AIAA J 1971;9:114–21.
[2] Jameson A, Schmidt W, Turkel E. Numerical simulation of the Euler equations by finite volume method using Runge–Kutta time-stepping schemes. AIAA Paper No. 81-1259, Fifth AIAA Computational Fluid Dynamics Conference, 1981.
[3] Jameson A. Solution of the Euler equations for two-dimensional transonic flow by a multigrid method. Appl Math Comput 1983;13:327–55.

[4] Spekreijse S. Multigrid solution of monotone second-order discretization of hyperbolic conservation laws. Math Comp 1987;49:135–55.
[5] Sidilkover D. Numerical solution to steady-state problems with discontinuities. PhD Thesis, The Weizmann Institute of Science, Rehovot, Israel, 1989.
[6] Sidilkover D, Brandt A. Multigrid solution to steady-state 2d conservation laws. SIAM J Numer Anal 1993;30:249–74.
[7] Sidilkover D. A genuinely multi-dimensional upwind scheme for the compressible Euler equations. In: Glimm J, Graham MJ, Grove JW, Plohr BJ, editors. Proceedings of the Fifth International Conference on Hyperbolic Problems: Theory, Numerics, Applications. Singapore: World Scientific; June 1994.
[8] Sidilkover D. A genuinely multi-dimensional upwind scheme and efficient multigrid solver for the compressible Euler equations. ICASE Report No. 94-84, NASA Langley Research Center, Hampton, VA, USA, 1994.
[9] Sidilkover D. Multi-dimensional upwinding and multigrid. AIAA 95-1759, 12th AIAA CFD meeting, San Diego, 19–22 June, 1995.
[10] Brandt A. Multigrid techniques: 1984 guide with applications to fluid dynamics. The Weizmann Institute of Science, Rehovot, Israel, 1984.
[11] Brandt A, Yavneh I. On multigrid solution of high-Reynolds incompressible entering flows. J Comput Phys 1992;101:151–64.
[12] Rosenfeld M, Israeli M. Numerical solution of incompressible flows by a marching multigrid nonlinear methods. AIAA J 1987;25:641–7.
[13] Sidilkover D, Ascher U. A multigrid solver for the steady-state Navier–Stokes equations using the pressure-Poisson formulation. Matematica Aplicada e Computational 1995;14:21–35.
[14] Roberts TW, Sidilkover D, Swanson RC. Textbook multigrid efficiency for the steady Euler equations. AIAA Paper No. 97-1949, 13th AIAA CFD Conference, Snowmass Village, CO, June–July 1997, A Collection of Technical Papers, Part 2, p. 629–36.
[15] Roberts TW, Swanson RC, Sidilkover D. An algorithm for ideal multigrid convergence for the steady Euler equations. Comput Fluids 1999;28:427–42.
[16] Roberts TW, Swanson RC. Extending ideally converging multigrid methods to airfoil flows. AIAA Paper No. 99-3337, 1999, 14th AIAA CFD Conference, Norfolk, VA, June–July 1999.
[17] Sidilkover D. Some approaches towards constructing optimally efficient multigrid solvers for the inviscid flow equations. Comput Fluids 1999;28:551–71.
[18] Sidilkover D. Factorizable schemes for the equations of fluid flow. Report No. 99-20, ICASE, 1999; Appl Numer Math, in press.
[19] Sidilkover D. The UHF scheme in two- and three-dimensions. SIAM J Numer Anal, 1999, submitted for publication.
[20] Sidilkover D, Roberts TW, Thomas JL. The generalized coordinate formulation of the UHF scheme. J Comp Phys, 1999, submitted for publication.
[21] Tsynkov SV. Numerical solution of problems on unbounded domains. A review. Appl Numer Math 1998;27:465–532.
[22] Ryaben'kii VS. Boundary equations with projections. Russian Math Surveys 1985;40:147–83.
[23] Ryaben'kii VS. Difference potentials method for some problems of continuous media mechanics. Moscow: Nauka; 1987 [Russian].
[24] Ryaben'kii VS. Difference potentials method and its applications. Math Nachr 1996;177:251–64.
[25] Ryaben'kii VS, Tsynkov SV. Artificial boundary conditions for the numerical solution of external viscous flow problems. SIAM J Numer Anal 1995;32:1355–89.
[26] Tsynkov SV. An application of nonlocal external conditions to viscous flow computations. J Comput Phys 1995;116:212–25.
[27] Tsynkov SV, Turkel E, Abarbanel S. External flow computations using global boundary conditions. AIAA J 1996;34:700–6.
[28] Tsynkov SV. Artificial boundary conditions for computation of oscillating external flows. SIAM J Sci Comput 1997;18:1612–56.

[29] Ryaben'kii VS, Tsynkov SV. An application of the difference potentials method to solving external problems in CFD. In: Hafez M, Oshima K, editors. Comput Fluid Dyn Rev, Singapore: World Scientific; 1998. p. 169–205.
[30] Tsynkov SV, Vatsa VN. An improved treatment of external boundary for three-dimensional flow computations. AIAA J 1998;36:1998–2004.
[31] Tsynkov SV. External boundary conditions for three-dimensional problems of computational aerodynamics. SIAM J Sci Comput 1999;21:166–206.
[32] Tsynkov SV. On the combined implementation of global boundary conditions with central-difference multigrid flow solvers. In: Geers TL, editor. Proceedings of IUTAM Symposium on Computational Methods for Unbounded Domains, Boulder, CO, July 1997, Dordrecht: Kluwer; 1998. p. 285–94.
[33] Tsynkov S, Abarbanel S, Nordström J, Ryaben'kii V, Vatsa V. Global artificial boundary conditions for computation of external flows with jets. AIAA J 2000;38:2014–22.
[34] Ferm L. Non-reflecting accurate open boundary conditions for the steady Euler equations. Technical Report no. 143, Department of Scientific Computing, Uppsala University, Uppsala, Sweden, September 14, 1992.
[35] Ferm L. Open boundary conditions for external flow problems. J Comput Phys 1990;91:55–70.
[36] Ferm L. Modified external boundary conditions for the steady Euler equations. Technical Report No. 153, Department of Scientific Computing, Uppsala University, Uppsala, Sweden, 25 August 1993.
[37] Ferm L. Multigrid for external flow problems. Technical Report, Department of Scientific Computing, Uppsala University, Uppsala, Sweden, 9 September 1993.
[38] Bayliss A, Goldstein CI, Turkel E. The numerical solution of the Helmholtz equation for wave propagation problems in underwater acoustics. Comput Math Appl 1985;11:655–65.
[39] Lončarić J. Optimal control of unsteady Stokes flow around a cylinder and the sensor/actuator placement problem. ICASE Report No. 98-18, NASA Langley Research Center, Hampton, VA, USA, May 1998.
[41] Wesseling P. An introduction to multigrid methods. Chichester: Wiley; 1992.